



Title	Dislocation mechanism for transformation between cubic ice I-c and hexagonal ice I-h
Author(s)	Hondoh, T.
Citation	Philosophical Magazine, 95(32), 3590-3620 https://doi.org/10.1080/14786435.2015.1091109
Issue Date	2015-09-01
Doc URL	http://hdl.handle.net/2115/62758
Rights	This is an Accepted Manuscript of an article published by Taylor & Francis in Philosophical Magazine on 1 September 2015, available online: http://www.tandfonline.com/doi/full/10.1080/14786435.2015.1091109
Type	article (author version)
File Information	Hondoh_PhiIMag2015(PDF_2 for HUSCAP).pdf



[Instructions for use](#)

Dislocation mechanism for transformation between cubic ice I_c and hexagonal ice I_h

T. Hondoh*† 

Institute of Low Temperature Science, Hokkaido University, N19W8 Sapporo, 060-0819 Japan

(Received 28 November 2014; accepted 1 September 2015)

Cubic ice I_c is metastable, yet can form by the freezing of supercooled water, vapour deposition at low temperatures, and by depressurizing high-pressure forms of ice. Its structure differs from that of common hexagonal ice I_h in the order its molecular layers are stacked. This stacking order, however, typically has considerable disorder; that is, not purely cubic, but alternating in hexagonal and cubic layers. In time, stacking-disordered ice gradually decreases in cubicity (fraction having cubic structure), transforming to hexagonal ice. But, how does this disorder originate and how does it transform to hexagonal ice? Here we use numerical data on dislocations in hexagonal ice I_h to show that (1) stacking-disordered ice (or I_c) can be viewed as fine-grained polycrystalline ice with a high density of extended dislocations, each a widely extended stacking fault bounded by partial dislocations, and (2) the transformation from ice I_c to I_h is caused by the reaction and motion of these partial dislocations. Moreover, the stacking disorder may be in either a higher stored energy state consisting of a sub-boundary network arrangement of partial dislocations bounding stacking faults, or a lower stored energy state consisting of a grain structure with a high density of stacking faults but without bounding partial dislocations. Each state transforms to I_h differently, with a duration to fully transform that strongly depends on temperature and crystal grain size. The results are consistent with the observed transformation rates, transformation temperatures, and wide range in heat of transformation.

Key words: cubic ice; stacking fault; partial dislocation; phase transformation

*Email: hondoh@general.hokudai.ac.jp

†Present address: Professor emeritus at Hokkaido University, 2-2-107, 5-8 Hassamu, Nishi-ku Sapporo, 063-0825 Japan.

1. Introduction

It has been proposed that cubic ice I_c plays an important role in various natural phenomena such as cloud formation in the atmosphere [1-8] and crystallization from amorphous ice in astrophysical processes [8-10]. But, I_c is not a stable form of ice; it spontaneously transforms into stable hexagonal ice I_h as it grows. Fundamentally, the chemical potential of I_c exceeds that of I_h at all temperatures, but its smaller interfacial energy allows its formation free energy to be less than that of I_h for crystals smaller than a critical size [11], meaning any cubic crystals larger than this critical size would necessarily be transient. For a supercooled water droplet to freeze as I_c , the calculated critical radius is as small as about 15 nm [12].

But the critical-radius argument does not explain recent findings in which I_c crystals form by depressurization of high-pressure forms of ice. In these cases, the crystals are randomly oriented polycrystalline aggregates with grains as small as several 10s of nanometres [1,13]. The critical-radius argument, being based on morphological stability due to difference in interfacial energies of low-indices lattice planes such as $\{111\}$ of I_c , and (0001) and $\{10\bar{1}0\}$ of I_h , does not apply because polycrystalline aggregates do not exhibit such morphological characteristics. Therefore some other mechanism is needed to explain why the I_c structure appears in such polycrystalline aggregates.

Cubic ice crystals, much larger than the above critical size, have been studied using x-ray and neutron diffraction, and found to have stacking disorder in one dimension [1,2]. Kuhs et al. used the term “ice I_c ”, adding quotes to reflect deviations from the cubic symmetry [1], and Malkin et al. referred to this ice as stacking-disordered ice I_{sd} [2,14]. Recently, the term I_{ch} was proposed as more appropriate for this ice [13,15].

The stacking disorder can be viewed as a particular arrangement of stacking faults lying on basal planes in hexagonal ice I_h . Thus the formation of I_c , followed by the transformation to I_h can be understood as the generation and then annihilation of these faults. These processes occur via the motion of partial dislocations, so the main problem here is to understand how the nature and behaviour of the partial dislocations in I_h leads to the observed features of cubic ice. These observations include the formation of the stacking-disordered state, wide scattering in enthalpy of transformation (13–50 J/mol depending on the method by which the I_c crystal was formed [16]), and an exothermic transformation during stepped heating for about one day from 165 to 225 K [17].

In the present paper, I describe how the motion of partial dislocations can (1) produce the stacking-disordered state in ice I_h and (2) lead to the observed transformation from I_c to I_h . In particular, formation of the stacking-disordered state can be explained through the characteristic nature of widely extended dislocations on basal planes in I_h , whereas the transformation to I_h can be explained via two steps, the first step being relatively fast, occurring through a glissile Shockley partial dislocation, and the second through a sessile Frank–Shockley partial dislocation. The transformation mostly occurs in the first step, but cannot be completed without the second.

We use the hexagonal system here to express the crystallographic planes and axes instead of the cubic one, because the formation and transformation mechanism developed here is easier to describe using dislocation dynamics in hexagonal ice I_h . In addition, for

1 simplicity, we use the following notation for the crystallographic directions: ‘ \mathbf{a} ’ for
 2 $(1/3)\langle 11\bar{2}0 \rangle$, ‘ $\mathbf{a}+\mathbf{c}$ ’ for $(1/3)\langle 11\bar{2}3 \rangle$, ‘ \mathbf{c} ’ for $\langle 0001 \rangle$, ‘ \mathbf{p}_i ’ for $(1/3)\langle 10\bar{1}0 \rangle$, and ‘ $\mathbf{p}_i+\mathbf{c}/2$ ’ for
 3 $(1/6)\langle 20\bar{2}3 \rangle$, and the terms for the crystallographic planes as ‘basal plane’ for $\langle 0001 \rangle$,
 4 ‘prismatic plane’ for $\{10\bar{1}0\}$ or $\{11\bar{2}0\}$, and ‘pyramidal plane’ for $\{10\bar{1}1\}$ or $\{11\bar{2}2\}$.

5 Numerical calculations in the following section were done using the mathematical
 6 software Calking-12 by Simplex Inc.

8 **2. Dislocation model for the transformation between I_c and I_h**

9 **2.1. Background (1): Relevant partial dislocations and stacking faults**

10
 11 The two crystal structures differ in their stacking sequence, as shown in Figure 1. The
 12 hexagonal I_h has a periodic stacking sequence of two bilayers, labelled ‘ A ’ and ‘ B ’,
 13 whereas I_c has three bilayers, labelled ‘ A ’, ‘ B ’, and ‘ C ’. As we use the hexagonal crystal
 14 nomenclature, it is clearer to first describe the transformation from hexagonal to cubic.

15 To see how this transformation can occur by the glide motion of a partial dislocation,
 16 consider a cut plane S parallel to the basal plane as shown in Figure 1(a). Now, shear the
 17 top half relative to the bottom half by glide motion of a dislocation with Burgers vector \mathbf{p}_i ,
 18 as shown in Figure 1(c). Then, the bilayer A just above S is turned into the new bilayer C ;
 19 that is, the stacking sequence changes to ABC of I_c from AB of I_h . As the translation vector
 20 (or the Burgers vector) \mathbf{p}_i is not a lattice vector of I_h , the shear plane S in Figure 1(b) is
 21 called a stacking fault, and this type of dislocation is called a partial dislocation to
 22 distinguish it from a perfect dislocation with a Burgers vector equal to a lattice vector (such
 23 as \mathbf{a} in Figure 1(c)). Although this process shows the transformation from I_h to I_c , it can be
 24 reversed, transforming I_c into I_h by the glide motion of the same dislocation.

25 As this shear displacement changes all of the A and B bilayers above plane S into C
 26 and A , the stacking sequence after the shear displacement can be expressed by
 27 $AB|CACA\dots$, with the symbol ‘|’ marking the stacking fault location. Then, as the same
 28 type of stacking fault would change C to B , introducing the stacking fault in every other
 29 bilayer would produce the sequence $AB|CA|BC|AB|C\dots$, which is the cubic stacking
 30 sequence. That is, I_c can be regarded as a particular state of I_h that includes a regular
 31 arrangement of stacking faults. Consequently, we can view the transformation from I_c to I_h
 32 as an annihilation process of stacking faults that lie on ice I_h basal planes. When all faults
 33 are removed, we are left with pure ice I_h .

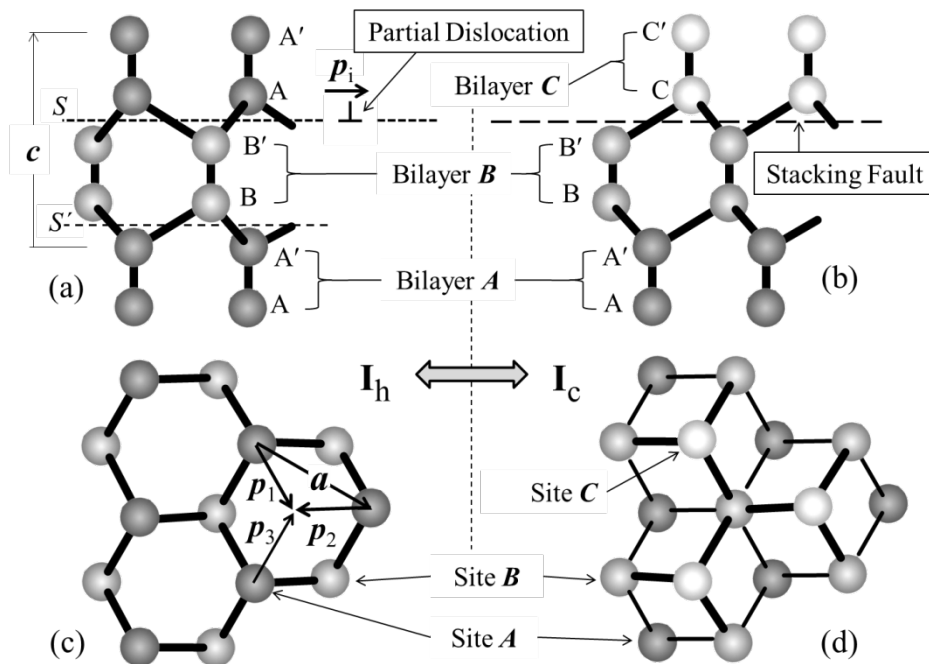
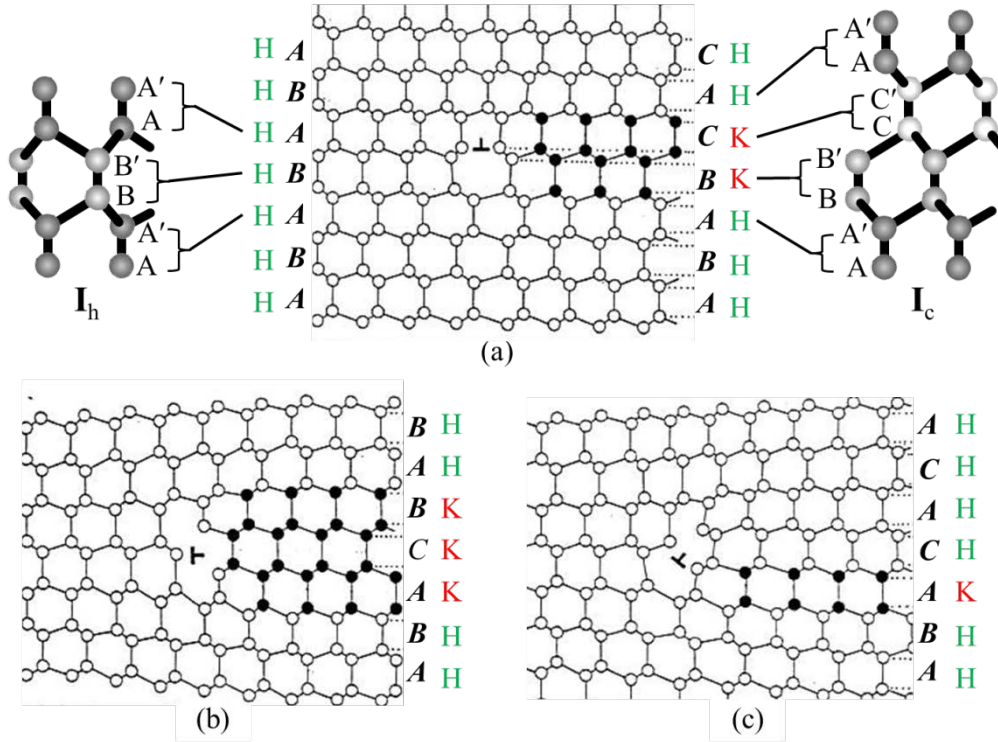


Figure 1. A dislocation mechanism for the reversible transformation between hexagonal ice I_h and cubic ice I_c . Balls and sticks show the oxygen atoms and the hydrogen bonds, respectively: (a) and (c) for the I_h structure projected on a prismatic plane $\{11\bar{2}0\}$ and on a basal plane, respectively, and (b) and (d) for the corresponding projections of the I_c structure. Bimolecular layers A-A', B-B' and C-C' are simply designated bilayers A, B, and C, respectively. Reversible transformation between I_h and I_c can be made by glide motion of a partial dislocation with a Burgers vector p_i ($i=1, 2$ or 3) along the basal slip plane S between the bilayers A and B. The bilayer A turns into a new bilayer C by this glide motion, transforming I_h to I_c , and *vice versa* for the transformation from I_c to I_h . The same transformation occurs by the glide motion along the slip plane S' although the arrangement of partial dislocations differs from S as shown in Figure 9.

This annihilation process takes place by the partial dislocations moving along the basal planes. We consider here just the three lowest-energy partial dislocations. These three, shown in Figure 2, are energetically preferred due to their having the smallest Burgers vector b in each direction (parallel, perpendicular and inclined to the basal plane) [18,19]. The partial dislocation shown in Figures 1 and 2(a) has its Burgers vector parallel to the basal stacking-fault plane, making it a Shockley partial dislocation due to it being glissile on the basal plane. In contrast, the Frank and Frank-Shockley partial dislocations shown in Figures 2(b) and (c) are sessile because they require mass transport (due to their extra half bilayers) to move along the basal plane, and thus move much slower than the Shockley partial dislocation.



1
2
3
4
5
6
7
8
9
10
11
12
13

Figure 2. Stacking faults and relevant partial dislocations in ice I_h . (a) Shockley partial dislocation with Burgers vector p_i (i.e. $(1/3) \langle 01\bar{1}0 \rangle$) parallel to the stacking-fault plane as for Figure 1; i.e., being glissile. (b) Frank partial dislocation with Burgers vector $c/2$ (i.e. $(1/2) \langle 0001 \rangle$) normal to the stacking-fault plane. (c) Frank-Shockley partial dislocation with Burgers vector $c/2 + p_i$ (i.e. $(1/6) \langle 02\bar{2}3 \rangle$) inclined to the stacking-fault plane. Both (b) and (c) are sessile because those Burgers vectors are not parallel to the stacking fault (basal) plane (i.e., mass transport is required to move these dislocations). Small filled- and open-circles indicate oxygen atoms in the cubic and hexagonal structure, respectively. A , B and C attached to each bilayer corresponds to that in Figure 1. H and K represent the hexagonal and cubic sequence, respectively. An H-bilayer is always sandwiched by the same bilayers A , B or C , whilst a K-bilayer is sandwiched by different bilayers.

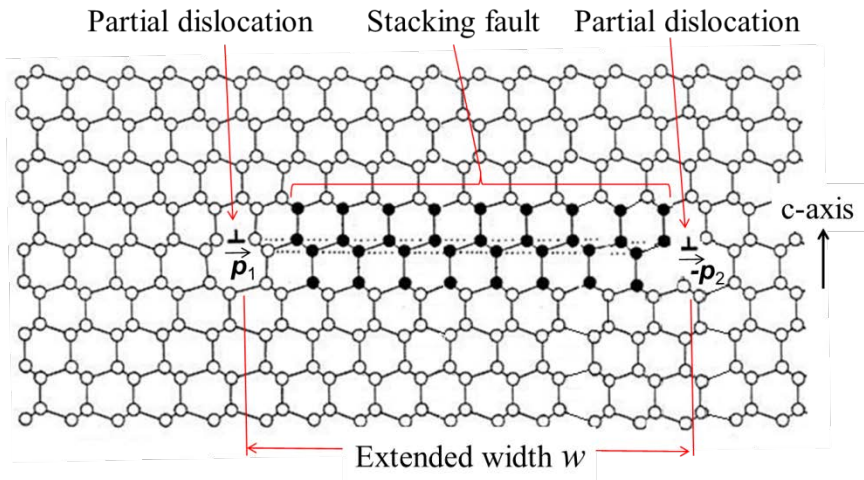
14
15
16
17
18
19
20
21
22
23
24
25
26
27

Consider the stacking-fault energies. By measuring the shrinkage rates of dislocation loops in I_h , the stacking-fault energy γ_{f1} for the Frank-Shockley type shown in Figure 2(c) was determined to be $0.31 \times 10^{-3} \text{ J/m}^2$ [20]. No measurements were done for the other two stacking-fault types. To estimate these energies, we consider the bilayers. The solid-black circles in Figure 2 show the cubic-stacking bilayers associated with these partial dislocations. Following Kuhs et al. [1], cubic bilayers are denoted K and hexagonal-stacked bilayers H. An H-bilayer is that which lies between two identical bilayers (e.g. a C between two A s), whereas a K-bilayer is sandwiched between different bilayers. Now assume that the corresponding energy for the other stacking-fault types scales with the number of K-bilayers. Using these numbers from Figure 2, we find a stacking-fault energy for the Shockley-type $\gamma_{f2} = 0.62 \times 10^{-3} \text{ J/m}^2$ and the Frank-type $\gamma_{f3} = 0.93 \times 10^{-3} \text{ J/m}^2$. The measurements were done at $-20 \text{ }^\circ\text{C}$, and without further knowledge of their temperature dependence, we assume they provide a good approximation for lower temperatures as well.

1
2
3 **2.2. Background (2): Extended dislocations**

4 The stacking fault described above has a small enough energy to stabilize all types of
5 dislocations in ice I_h by dissociating into two partial dislocations lying on a basal plane.
6 This type of dislocation is called an extended dislocation; specifically, to become stable, a
7 perfect dislocation with Burgers vector \mathbf{a} turns into a stacking fault bounded by two
8 Shockley partial dislocations with Burgers vector \mathbf{p}_1 and \mathbf{p}_2 ($\mathbf{a} = \mathbf{p}_1 - \mathbf{p}_2$ in Figure 1) as
9 shown in Figure 3 [18, 19]. This structure allows frequent local switching between I_h and I_c
10 during glide motion of the extended dislocations on basal planes in hexagonal ice I_h . Such
11 glide motion of extended dislocations play a key role in the plastic deformation of ice I_h
12 [18,19,21].

13 The width (w) of the extended dislocation in equilibrium w_e can be calculated by
14 equating the repulsive force between the two partial dislocations with the shrinkage force
15 due to the stacking fault energy. This width depends on the Burgers vector \mathbf{b} and the angle
16 ω between \mathbf{b} and the line vector \mathbf{l} of the associated perfect dislocation (e.g. [22]). The
17 calculated widths w_e for the Shockley type (Burgers vector \mathbf{a}) described above are 25 nm
18 for a screw perfect dislocation ($\omega = 0^\circ$), 49 nm for a 60° -perfect dislocation ($\omega = 60^\circ$) and
19 57 nm for an edge perfect dislocation ($\omega = 90^\circ$). In this calculation, we use
20 temperature-range-averaged constant values for lattice constants as $a = 0.451$ nm, $c =$
21 0.734 nm.
22



23
24 Figure 3. Extended dislocation. A perfect dislocation with Burgers vector \mathbf{a} dissociated into the
25 two Shockley partial dislocations that bound a stacking fault.
26

27 Much larger widths of w_e are obtained for both the Frank–Shockley type shown in
28 Figure 2(c) and the Frank type shown in Figure 2(b) because their Burgers vector lengths
29 exceed that of \mathbf{a} . For the Frank–Shockley type (Burgers vector $\mathbf{a} + \mathbf{c}$), these widths are 437
30 nm ($\omega = 0^\circ$ for \mathbf{a} component) and 566 nm ($\omega = 90^\circ$ for \mathbf{a} component), whereas for the
31 Frank type (Burgers vector \mathbf{c}), the width is 129 nm. As their generation and motion along
32 basal planes require mass transport, these dislocations are less important in
33 low-temperature processes, yet become active at higher temperatures [18,19]. For example,

1 these two types of dislocations are frequently observed as dislocation loops in ice I_h just
2 after growth from the melt and during heat treatment (either by cooling or heating) above
3 about 220 K [20,23-25].

4 5 **2.3. Formation mechanism of stacking-disordered state in hexagonal ice I_h**

6
7 Due to their very large extended widths, dislocations in ice I_h tend to align parallel to basal
8 planes. Consequently, most dislocations in well-aged or annealed ice I_h lie on basal planes,
9 with only short, segmented dislocations on non-basal planes [18,19,21]. As such, some
10 cubic stacking sequences exist even in stable hexagonal ice I_h , with a cubicity (fraction of
11 ice with cubic structure) proportional to the dislocation density. Generally, the cubicity is
12 very low; for example, an aged crystal of I_h may have a dislocation density of 10^8 – 10^{12} m^{-2} ,
13 yielding a cubicity of 10^{-8} – 10^{-4} , low enough to ignore.

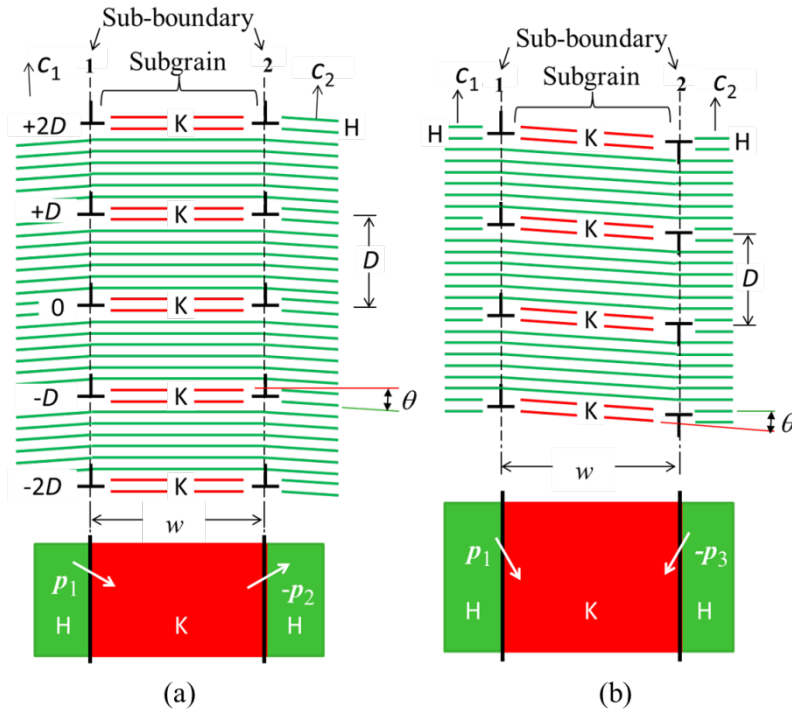
14 However, much larger cubicity may exist in polycrystalline ice I_h with very small
15 crystallite (grain) sizes. When a grain diameter is smaller than the equilibrium width w_e ,
16 the stacking faults extend over entire basal planes, resulting in a high fraction of K-bilayers.
17 Consider an ideal case in which perfect dislocations with Burgers vector \mathbf{a} are introduced
18 on every other bilayer (basal plane). Such a case results in pure cubic ice I_c because each
19 Shockley partial dislocation turns two bilayers from H to K as shown in Figure 2(a).
20 Assuming a grain size equal to the maximum extended-width of 57 nm for perfect
21 dislocations with Burgers vector \mathbf{a} , the resulting dislocation density is about 10^{16} m^{-2} .
22 Although much larger than that in well-aged ice, the dislocation density could be nearly
23 this high due to stress concentrations caused by the crystallization method, such as from
24 depressurization from a high-pressure phase of ice and from rapid freezing of water
25 droplets. In a real case, dislocations generated by such stress concentrations must be
26 randomly distributed on different basal planes, which would result in a mixture of I_h and I_c ,
27 or a stacking-disordered state of ice I_h .

28 Measured grain sizes are consistent with this formation mechanism. For cubic ice
29 formed by depressurization, Hansen et al. [13] reports grain sizes of 25 nm in both
30 directions parallel and perpendicular to the c -axis at the beginning of the transformation
31 from ice I_c to I_h . For vapour-deposited ice, Kuhs et al. [26] reported grain sizes of about 70
32 nm at the beginning of the transformation to I_h . Although the grain diameters are larger
33 than w_e for the Shockley type in this case, the stacking fault can extend more than w_e
34 because of the repulsive force between dislocations comprising an array, resulting in a
35 stacking-disordered state.

36 As these observed crystallite (grain) sizes are as small as the equilibrium extended
37 widths w_e for Burgers vector \mathbf{a} , the grain structure is likely an array of extended
38 dislocations. The arrays of edge and screw perfect dislocations turn into a sub-grain with a
39 mixed structure of I_h and I_c bounded by arrays of partial dislocations as shown in Figures
40 4(a) and (b). This dislocation array gives rise to a small change in the crystal orientation
41 across a layer. The array is also called a low-angle grain boundary, or sub-boundary.

42 This sub-grain structure is very different from those in other materials with higher
43 stacking-fault energies, where the sub-boundaries consist instead of perfect dislocations.
44 Even if the sub-boundaries are composed of extended dislocations, their separation widths
45 w are much smaller than sub-grain sizes. That is, in other materials, the set of two partial

1 dislocation arrays (sub-boundaries 1 and 2) would instead be considered a single low angle
 2 grain boundary (or a single sub-boundary), and thus contain no sub-grain. Thus, the
 3 particular sub-grain structure in Figure 4 becomes possible only with a material with very
 4 low stacking fault energy, such as ice I_h .
 5



6
 7 Figure 4. Dislocation arrays composed of the extended dislocations shown in Figure 3. (a) Edge
 8 perfect dislocation array extends to two 60°-partial dislocation arrays separated by w . D is the
 9 distance between the extended dislocations. The misorientation angle θ equals 4.4° and angle
 10 between c_1 and c_2 is 8.8°. (b) Screw perfect dislocation array extends to two 30°-partial
 11 dislocation arrays. The misorientation angle θ equals 2.5° and angle between c_1 and c_2 is 0°.
 12

13 As a result of this particular sub-grain structure, the widely extended screw dislocation
 14 array has a new sub-grain between the two partial dislocation arrays as shown in Figure
 15 4(b). Here the misorientation depends on the edge component of the Burgers vector of the
 16 partial dislocations. In particular, the misorientation angle θ for the tilt sub-boundary is
 17 $\theta \approx b_e / D$, where D is the partial dislocations' spacing, and b_e the edge component of the
 18 Burgers vector.

19 However, according to ordinary dislocation theory, the separation w decreases with
 20 increasing θ (i.e., decreasing D) for an array of extended dislocations (e.g. [22]). According
 21 to theory, as θ increases, the sub-grain shown in Figure 4 may disappear. However, the
 22 theory assumes an infinite number of extended dislocations. For a limited number of partial
 23 dislocations, the interaction forces between the arrays may noticeably change due to the
 24 sub-grain sizes being very small in the present case.

25 Consider the interaction force exerted on the partial dislocation located at '0' in
 26 sub-boundary 2 from other partial dislocations located at $\pm nD$ of sub-boundary 1 in

1 Figure 4(a). Using the edge and screw components of \mathbf{p}_i ($b_p \sin 60^\circ$, $b_p \cos 60^\circ$), the repulsive
 2 force (per unit length) parallel to the basal plane is

$$3 \quad f_N(w) = f_0(w) + \frac{\mu b_p^2}{4\pi} \left[\frac{3}{1-\nu} \sum_{n=1}^N \frac{w(w^2 - (nD)^2)}{(w^2 + (nD)^2)^2} - \sum_{n=1}^N \frac{w}{w^2 + (nD)^2} \right], \quad (1)$$

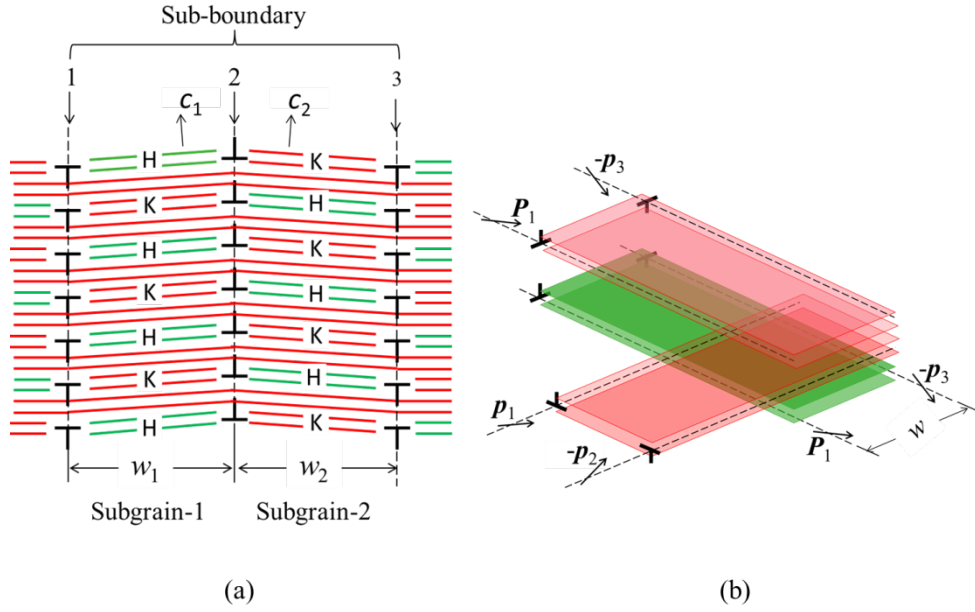
$$4 \quad f_0(w) = \frac{\mu b_p^2}{8\pi} \frac{2+\nu}{1-\nu} \frac{1}{w}$$

4 where $f_0(w)$ is the repulsive force between two partial dislocations separated by w on the
 5 same basal plane, μ the shear modulus, and b_p the Burgers vector length of \mathbf{p}_i . The
 6 separation in equilibrium w_{Ne} can be calculated by equating $f_N(w)$ to the stacking fault
 7 energy γ_2 . As $f_N(w)$ is approximately equal to $f_0(w)(2N+1)$ for $w \gg ND$, the separation
 8 w_{Ne} should roughly equal to w_e multiplied by the number of partial dislocations in the array.
 9 In the case of Figure 4(a) (i.e., $N=2$), for example, the equilibrium separation w_{Ne} equals
 10 $5w_e$ provided that $2D < 5w_e$. Thus, in contrast to the case with an infinite dislocation array,
 11 the stacking fault can extend much more than w_e as the sub-grain size increases.

12 For a very large N , by equating γ_2 and $f_N(w)$, we obtain two values of w_{Ne} . One value
 13 follows from the above approximation and the other value is close to that predicted by the
 14 dislocation theory. For the case $N \approx 100$ and $D \approx 8c$ (i.e. $\theta \approx 2.2^\circ$) in Figure 4(a), the values
 15 are about 20 μm and 5 nm. The former value is of no use because it is much larger than the
 16 size of the sub-grains. The latter solution, which is consistent with the prediction from
 17 dislocation theory, can be obtained only when $N \geq 100$, and the separation w becomes
 18 much smaller than w_e for sub-grain sizes larger than 1.2 μm .

19 The stacking disordered state can be thought of as an arrangement of extended
 20 dislocation arrays. Consider the arrangement in Figure 5. This arrangement, which gives
 21 maximum cubicity among all possible arrangements of dislocations, was made by
 22 interconnecting the sub-grain structure in Figure 4(b) with its mirror symmetry structure
 23 about the sub-boundary 1, and inserting other extended dislocations running different
 24 directions between the former extended dislocations. A 3-D view of the planes is shown in
 25 Figure 5(b). The misorientation angle between c_1 and c_2 equals about 10° because $b_e \approx 0.13$
 26 nm and $D \approx 0.73$ nm.

27 This arrangement gives a maximum cubicity of 0.75. Real ice would have more
 28 complicated configurations with smaller cubicity. Thus, the estimate is consistent with the
 29 reported values of initial cubicity of about 0.6 [1,13].
 30



1

2 Figure 5. Interconnecting extended dislocation arrays that maximize cubicity in the present
 3 dislocation model. (a) Two extended dislocation arrays shown in Figure 4(b) interconnecting with
 4 the third array as shown in (b).

5

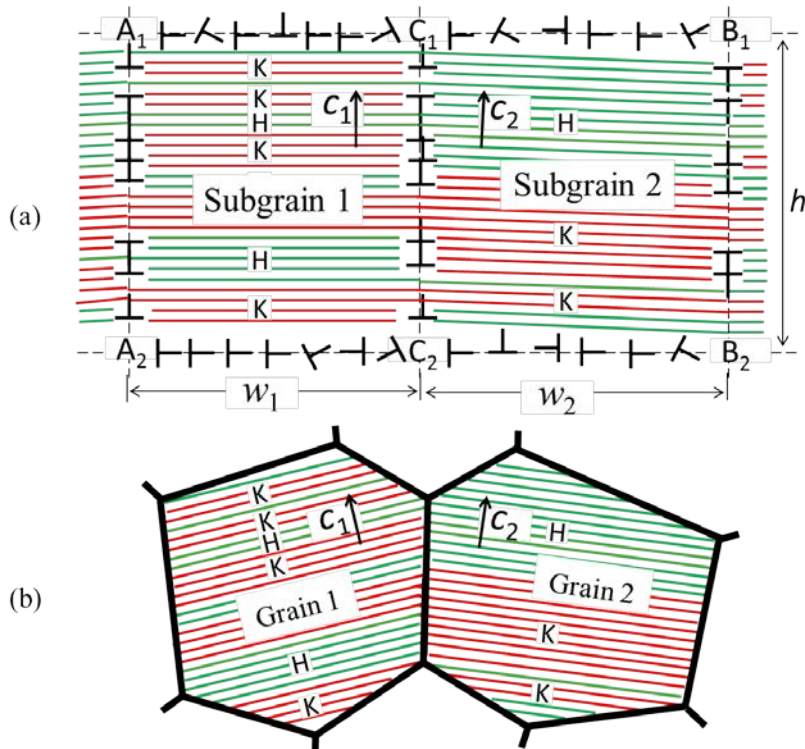
6 **2.4. Formation of sub-boundary structures**

7
 8 Consider first the formation of dislocations in ice. A rapid change of pressure or
 9 temperature (e.g. from depressurization or rapid freezing) causes large stresses in I_h that
 10 introduce many dislocations of all possible Burgers vectors [19,21]. In particular, a
 11 dislocation with Burgers vector \mathbf{a} , which plays a key role in plasticity of ice I_h , can be
 12 generated by uniaxial compression (or tension) inclined to the c -axis, but not by uniaxial
 13 deformation parallel to the c -axis; this case instead requires a dislocation with Burgers
 14 vector $\mathbf{a} + \mathbf{c}$. A dislocation with Burgers vector \mathbf{c} , on the other hand, can be generated only
 15 when a shear stress that is exerted on prismatic planes has a component parallel to the
 16 c -axis. Just after generation, all these dislocations must lie on their own slip planes.

17 At sufficiently low temperature, the dislocations do not climb, and thus only
 18 dislocations with Burgers vector \mathbf{a} can extend on basal planes or dissociate into Shockley
 19 partial dislocations. These partial dislocations rearrange into sub-boundaries normal to
 20 basal planes such as A_1A_2 , B_1B_2 , and C_1C_2 , resulting in a stacking disordered state as
 21 shown in Figure 6(a). In contrast, dislocations with Burgers vector $\mathbf{a} + \mathbf{c}$ or \mathbf{c} do not
 22 dissociate because their dissociation requires climb motion along basal planes, and such
 23 dislocations thus remain as perfect dislocations glissile on pyramidal or prismatic planes,
 24 respectively. These perfect dislocations rearrange into stable arrays (or sub-boundaries)
 25 parallel to basal planes such as A_1B_1 and A_2B_2 in Figure 6(a).

26 Such a sub-boundary structure will change to a lower energy configuration through
 27 dislocation reactions. These reactions include annihilation of dislocations with opposite

1 Burgers vectors, absorption and desorption of partial dislocations by arrays during
 2 sub-boundary migration, and sub-grain growth by annihilating sub-grains with a higher
 3 stored energy.
 4



5
 6
 7 Figure 6. Adjacent sub-grains and grains with stacking-disordered ice. (a) Subgrain structure
 8 bounded by partial dislocation arrays A_1A_2 , B_1B_2 , and C_1C_2 , and also perfect dislocation arrays
 9 A_1B_1 and A_2B_2 . (b) Adjacent grains structure with stacking disorder.

10
 11 **2.5. Modelling of the transformation from I_c to I_h**
 12

13 Consider the annealing (or ageing) of a stacking-disordered ice, or equivalently, a
 14 fine-grained polycrystalline ice with a high dislocation density. To reduce their stored
 15 energy, the dislocations rearrange and annihilate. During this process, the total area of the
 16 associated stacking faults decreases, transforming the ice to a stable state of ice I_h .

17 Thus, to model the transformation, we must model dislocation annihilation. Ideally,
 18 the modelling of such annihilation should consider the behaviour of high-density
 19 dislocations because their behaviour could differ from that of isolated single dislocations,
 20 as typically shown by dislocation avalanches in ice I_h [27]. We do not consider such
 21 complicated interactions here; instead, we just consider some probable dislocation
 22 mechanisms that can annihilate stacking faults.

23 Consider two cases for the initial state of the transformation: one in which all of the
 24 stacking faults are bounded by partial dislocations (Figure 6(a)), and the other in which
 25 stacking faults are bounded by high-angle grain boundaries with no partial-dislocations
 26 (Figure 6(b)). The former case would occur at low temperatures as described in the
 27 preceding section, resulting in either fewer dislocations or stable arrays. In the latter case,

1 the high-angle grain boundaries act as effective sinks for dislocations. To act as strong
2 sinks, the temperature should be relatively high. But for powdered ice, or generally when
3 there is only weak binding between the grains, the interface (or surface) can act as effective
4 sinks for dislocations even at low temperatures. Then, stacking faults will be swept out by
5 nucleation and motion of partial dislocations on the faulted planes. In either case, the
6 stacking faults are removed; in the former by sub-boundary migration, in the latter through
7 the motion of partial dislocations.

8 Although the processes in both cases would act simultaneously, we consider them
9 separately in the following sections.

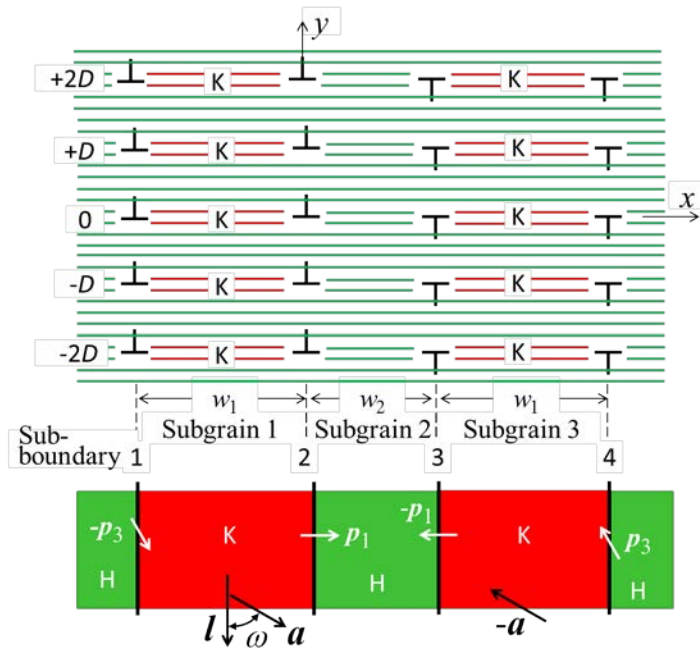
10 2.5.1. *Dislocation processes involved in the transformation*

11 Here, we consider the elemental dislocation processes that may be active in the
12 annihilation of stacking faults. The focus is on determining the temperature range in which
13 each relevant process becomes active.

14
15
16
17 2.5.1.1. *Glide motion of partial dislocations to annihilate dislocation arrays.* Extended
18 dislocation arrays consisting of two Shockley partial dislocations can be annihilated by
19 glide motion of the partial dislocations. Possible arrangement of this case, in which the
20 Burgers vectors \mathbf{a} and $-\mathbf{a}$ lie on the same basal plane, is shown in Figure 7. As the partial
21 dislocations comprising the sub-boundaries 2 and 3 have opposite Burgers vectors \mathbf{p}_1 and $-\mathbf{p}_1$,
22 glide motion on the same basal plane cause these two partial dislocations to quickly
23 annihilate each other, and then the partial dislocations composing the sub-boundaries 1 and
24 4 also annihilate each other to eliminate the stacking fault completely, resulting in a grain
25 only H-bilayers.

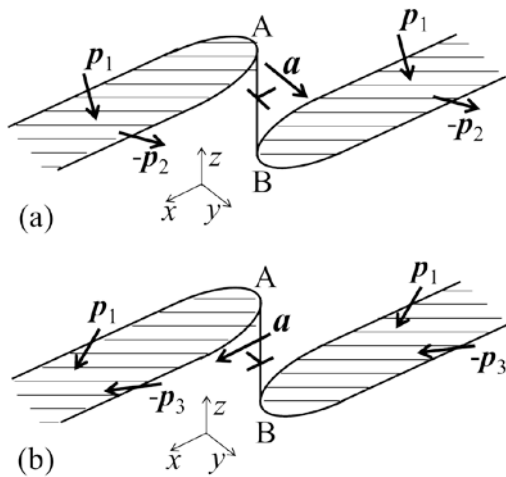
26
27 2.5.1.2. *Jogs and super jogs of extended dislocations.* In general, dislocations do not lie on
28 the same basal plane, instead having a jog or super jog. The jog slows the motion of a
29 dislocation because it requires mass transport. Consider the jogs in Figure 8. When the
30 height AB equals $c/2$, the shift is called a jog; when it is an integral multiple of $c/2$, it is
31 called a super jog. In the case of (b), climb motion is required to move the non-basal
32 segment AB in the direction parallel to y-axis together with those extended on basal planes,
33 whereas the case in (a) can move along y-axis without climb motion. Consequently, we
34 need to consider climb motion even in the case shown in Figure 7 if those dislocations
35 have jogs or super jogs.

36
37 2.5.1.3. *Climb motion of extended dislocations to annihilate dislocations with opposite*
38 *Burgers vectors.* Consider now the case in which two extended dislocations with opposite
39 Burgers vectors lie on different basal planes separated by distance D . Figure 9 shows two
40 examples: (a) with slip plane S from Figure 1, in which D equals an integral multiple of c ,
41 and (b) with slip plane S' , in which D equals a half-integral multiple of c . In both cases,
42 climb motion is required to move the extended dislocations normal to basal planes.
43 However, stacking faults prevent climb motion of partial dislocations, and therefore double
44 jog formation is required.



1
2
3
4
5
6

Figure 7. Sub-boundary arrangement with dislocations of opposite Burgers vectors that will be annihilated by glide motion. The edge and screw components of the partial dislocations depend on the angle ω between the line vector l (unit vector parallel to the dislocation line) and the Burgers vector a of the perfect dislocation.



7
8
9
10
11

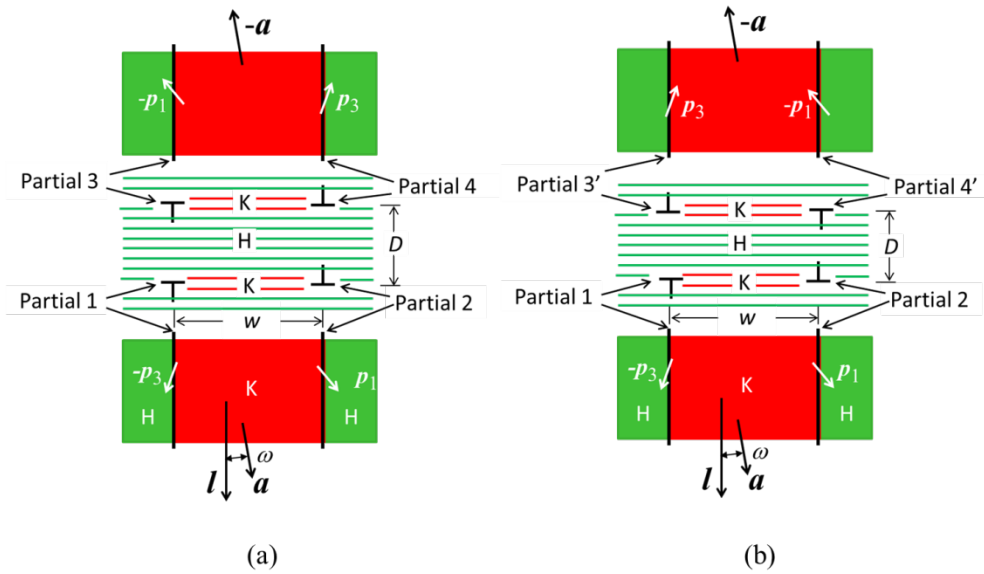
Figure 8. Jog on an extended dislocation. (a) Glissile jog for the motion in the y direction. (b) Sessile jog in the y direction, but glissile in the x direction. When the jog is longer than one layer long, it is a super jog.

12
13
14
15
16
17

Climb motion can proceed through double jog formation. First a short part of the extended dislocation shrinks to a perfect dislocation (Figure 10(a)), and then it can bow out due to an attractive force from partial dislocations (i.e., 3 and 4, or 3' and 4' in Figure 9). In general, double jog formation via constriction of an extended dislocation rarely occurs because the recombination of two partial dislocations has a high activation energy [28]. However, this activation energy can be lowered if the bow-out, such as $B'A_0A'AB$ shown

1 in Figure 10(b), is formed at a geometrical jog A_0B' . Then, climb of the segment AA' in the
 2 z direction can take place as the lateral motion of the segment AB proceeds. When AA'
 3 comes within a distance D of the lower fault plane, it dissociates into two partial
 4 dislocations. Then, as shown in Figure 10(c), two dislocation dipoles are formed when the
 5 overlapped part annihilates. If the Burgers vector of the super jogs (AB and $A'B'$) is
 6 parallel to the x -axis ($\omega = 0^\circ$ in Figure 9), the super jogs can glide on a non-basal plane to
 7 completely annihilate the stacking faults. In this special case, the bow-out in Figure 10(b)
 8 can move on a prismatic plane without climb motion, resulting in much faster annihilation
 9 of stacking faults than in the general cases (i.e., $\omega \neq 0^\circ$).

10



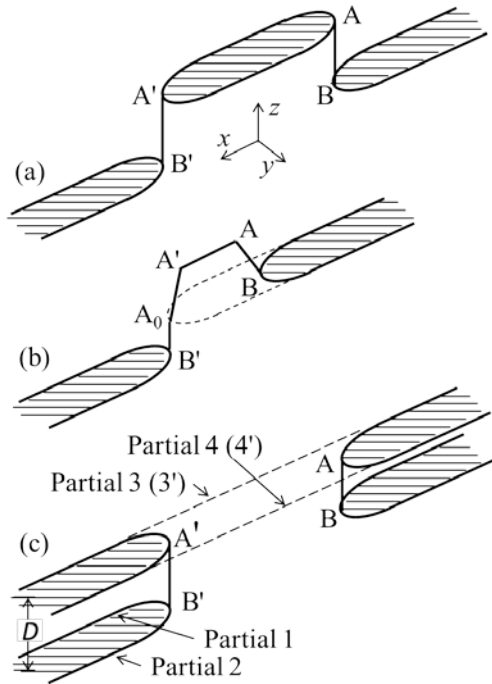
11

12 Figure 9. Extended dislocations with opposite Burgers vectors to be annihilated by climb
 13 motion. Two extended dislocations at a distance D that equals (a) an integral multiple of c , and (b)
 14 a half-integral multiple of c .

15

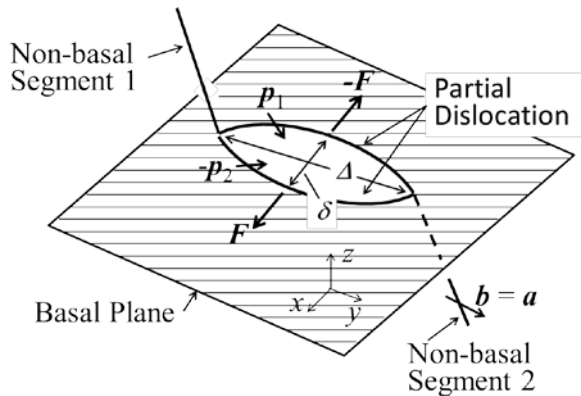
16 *2.5.1.4. Dissociation of a perfect dislocation inclined to the basal plane.* Dissociation on
 17 the basal plane is energetically favoured by all types of perfect dislocations lying on not
 18 only the basal plane but also inclined to the basal plane. Thus, a pair of partial dislocations
 19 can be generated from perfect dislocations that formed with the ice. One possible
 20 configuration of such partial dislocations is shown in Figure 11. This figure shows how a
 21 perfect dislocation inclined to the basal plane extends to a spindle-shaped configuration on
 22 the basal plane of a stacking fault to reduce the total energy. In this case, unlike the
 23 extended dislocations described in subsection 2.2, the outside is faulted, but there is no
 24 fault between the two partial dislocations, Therefore, no attractive force is exerted between
 25 the two partial dislocations although the curvature of the partial dislocations tends to shrink
 26 the extended configuration. Then, the two partial dislocations move apart, increasing both
 27 δ and Δ (Figure 11), and finally the non-basal segments may be absorbed by the grain
 28 boundary or interface, resulting in two parallel partial dislocations on the basal plane as
 29 shown in Figure 12(b). These two partial dislocations then move apart and annihilate the
 30 stacking fault. In addition to this process, a half loop of partial dislocation can be also

1 generated from this spindle-like configuration if it forms close to the grain boundary or
 2 interface as also shown in Figure 12(b).



3

4 Figure 10. Annihilation of extended dislocations by climb. (a) Double jog formation. (b) Climb
 5 motion of constricted perfect dislocation. (c) Formation of dislocation dipoles to annihilate the
 6 extended dislocations shown in Figure 9.

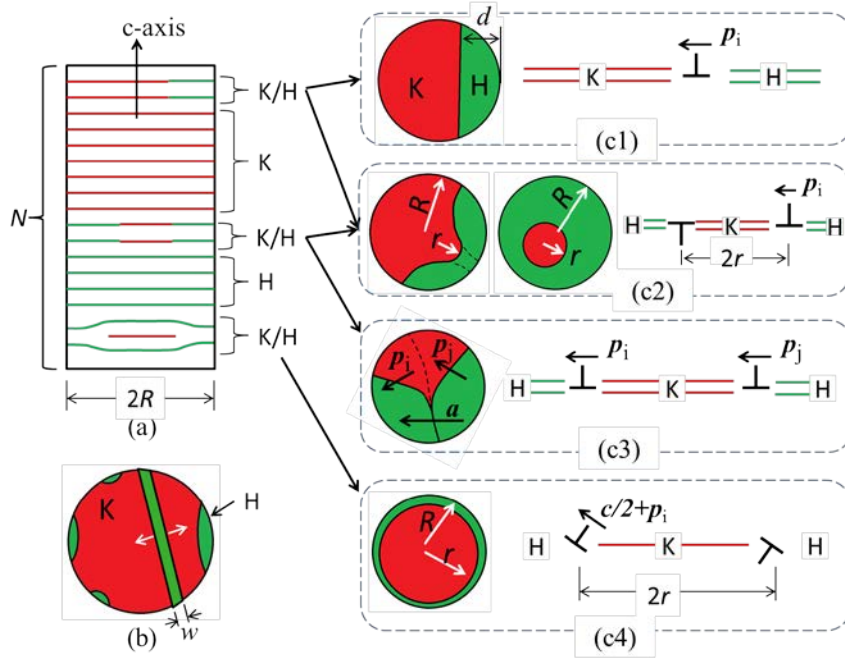


7

8 Figure 11. Dissociation of a skewed perfect dislocation on the basal plane.

9

10 **2.5.1.5 Mobility of Shockley partial dislocations.** For glide motion of a Shockley partial
 11 dislocation, we estimate the mobility using the data in references a basal plane [18]. This
 12 data was obtained by velocity measurements on isolated perfect-dislocations with Burgers
 13 vector \mathbf{a} that extend to the stacking fault bounded by two Shockley partial dislocations
 14 lying on a basal plane. Although interaction forces between dislocations moving on
 15 different basal planes may affect the dislocation motion (as in a dislocation avalanche [27]),
 16 we assume a linear relationship between the average dislocation velocity and the driving



1

2 Figure 12. Transformation of a cylindrical grain of cubic ice to hexagonal ice. (a) Side view of a
 3 transient state having a mixture of H-bilayers (hexagonal bilayers) and K-bilayers (cubic bilayers).
 4 N is the total number of bilayers. The bilayer separation equals to $c/2$. Here, K, H and K/H denote
 5 pure K-bilayers, pure H-bilayers, and K-bilayers partly transformed to H-bilayers, respectively. (b)
 6 Cross-section showing an initial stage of the transformation with nucleation of partial dislocations
 7 from the interface. (c1) A straight Shockley partial dislocation lying along the Peierls trough
 8 (G-line). (c2) A curved or looped Shockley partial dislocation (G-loop). (c3) A pair of Shockley
 9 partial dislocations with different Burgers vectors p_i and p_j ($i \neq j$). Each of these Shockley partial
 10 dislocations in (c1)–(c3) transforms two bilayers from K to H. (c4) A Frank–Shockley partial
 11 dislocation loop (C-loop) with Burgers vector $c/2 + p_i$ that annihilates an isolated K-bilayer.
 12 Although it is shown by a line here, the perfect dislocation with Burgers vector a is actually an
 13 extended dislocation with a width w_e .

14

15 force obtained by the above mentioned experiments. In this case, the Shockley partial
 16 dislocation glides at average velocity V_g on the basal plane, with magnitude proportional to
 17 the shear stress τ applied on the dislocation:

18

$$V_g = M \tau = M \frac{f}{b}, \quad (2)$$

$$M = M_0 \exp\left(-\frac{E_g}{kT}\right),$$

19 where E_g and $M_g = M/b$ are the activation energy and the mobility for the glide motion, and
 20 $f = \tau b$ is a force per unit length of dislocation.

21 Since a curved dislocation moves faster than a straight one sitting along the Peierls
 22 trough, we consider two values for the mobility M_g (or M). As a lower bound for M (i.e.,
 23 for the case of straight dislocation along the Peierls trough), E_g and M_0 are 0.756 eV and
 24 3.0×10^3 m/s·Pa, respectively [29]. By reanalyzing the velocity data of curved dislocations

1 with the Burgers vector \mathbf{a} in the temperature range 254–270 K from reference [30], E_g and
2 M_0 for curved Shockley partial dislocations are 0.624 eV and 14.5 m/s·Pa, respectively. The
3 latter value is used here as an upper bound for the mobility. In this calculation, the M_0
4 value for a Shockley partial dislocation is assumed to be twice that for a perfect dislocation
5 because a curved perfect dislocation would dissociate into two partial dislocations with the
6 same mobility [31].

7 We must pay careful attention to extrapolation of the mobility data to lower
8 temperatures because point defects, such as Bjerrum defects and self-interstitials, with
9 different activation energies for their formation and motion may affect the dislocation
10 mobility at low temperatures. However, the diffusion coefficients for proton transfer over a
11 wide temperature range of about 190–260 K are consistent with those of self-interstitials
12 above 220 K [32]. Therefore, we assume that the values of E_g and M_0 obtained above 250
13 K provide a good approximation for lower temperatures as well.

15 2.5.2. Transformation through sub-grain growth

16 Upon annealing (or ageing), stacking faults can be annihilated through motion of the
17 sub-boundaries (e.g. Figure 6(a)). Such motion is a key part of sub-grain growth, and thus
18 is a key process during the recovery of deformed crystals (e.g. [33]). Subgrain growth is
19 largely driven by the energy stored in sub-boundaries. However, the energy of a
20 sub-boundary strongly depends on the misorientation angle of adjacent sub-grains, which
21 is not constant during annealing (or ageing). In addition, the mobility of a sub-boundary
22 increases with increasing misorientation angle, but the average misorientation angle
23 decreases during sub-grain growth. Such factors make it difficult to formulate the growth
24 process of sub-grains. So, instead, here we focus on the dominant processes that transform
25 K-bilayers to H-bilayers in the sub-grain structure composed of a particular arrangement of
26 partial dislocations.
27

28 If a specimen has a sub-grain structure such as that in Figure 7, the mechanism
29 described above will remove all extended dislocations as well as stacking faults. As a result,
30 the number of sub-grains will decrease. Thus, the average sub-grain size increases as the
31 cubicity decreases, in agreement with measurements [13]. However, real arrangements
32 must include some disorder in the arrangement of partial dislocations and stacking faults
33 such as that shown in Figure 6(a). Nevertheless, because interaction forces between
34 sub-boundaries must be large enough for their migration in very small sub-grains,
35 coalescence of sub-boundaries may take place even in such a complicated sub-boundary
36 structures.

37 Such reactions between sub-boundaries may result in not only growth of sub-grains
38 but also sparser distribution of partial dislocations in the sub-boundaries. When this occurs,
39 the interaction forces that constrain the array decrease, allowing some partial dislocations
40 to release from their sub-boundary, bringing the extension closer to the equilibrium width
41 w_e . Subsequently, the particular sub-boundary network either breaks up into randomly
42 distributed extended dislocations or a normal sub-boundary network composed of perfect
43 dislocations. Either way, the resulting cubicity would be consistent with that in stable ice
44 I_h .

1 Among various dislocation processes described above, the fastest transformation
2 would occur through glide motion of Shockley partial dislocations in the sub-grain
3 structure. The slowest transformation, in contrast, would occur from the arrangement of
4 extended dislocations shown in Figure 9. The slower rate occurs because the annihilation
5 of partial dislocations and stacking faults involves climb motion of the constricted perfect
6 dislocations. A general mix of dislocation processes would result in various transformation
7 rates between these fast and slow cases.

9 2.5.3. Transformation through annihilation of stacking faults

10
11 If the partial dislocations that bound the stacking faults are absorbed by the grain boundary,
12 the stacking faults extend across the entire grain (e.g. Figure 6(b)). Such a grain structure
13 can be obtained as a result of the sub-grain growth described above because a sub-grain
14 structure could be included in each grain as its substructure. And if the Shockley-type
15 stacking faults are laid out on every other basal plane, the grain would be pure (ideal) cubic
16 ice I_c . In this case, to transform to stable ice I_h upon annealing, stacking faults must be
17 gradually annihilated by nucleation and motion of partial dislocations.

18 Consider an intermediate state in the transformation, that is, a mixed state of H- and
19 K-bilayers. An example is in Figure 12(a) which corresponds to a grain in Figure 6(b). For
20 the transformation of complete K-bilayers to H-bilayers, half loops of partial dislocations
21 must nucleate at the grain boundary or interface, as in Figure 12(b), because only at the
22 grain boundary or interface can there be sufficient irregularities to allow dislocation
23 nucleation. Then, the partial dislocations sweep inward, transforming K-bilayers to
24 H-bilayers. The nucleated partial dislocations are most likely the Shockley-type because
25 only this type is glissile or requires no mass transport for nucleation and motion. By a
26 Shockley partial dislocation sweeping inward, two K-bilayers are transformed into two
27 H-bilayers as shown in (c1) of Figure 12.

28 When two such Shockley partial dislocations meet in the interior, two things can
29 happen. If their Burgers vectors differ (e.g. one is p_1 , the other p_2 in Figure 1), then a
30 perfect dislocation with Burgers vector a (equal to $p_1 - p_2$) is formed as shown in Figure
31 12(c3). If instead their Burgers vectors are the same, they turn into a single Shockley
32 partial dislocation or a circular loop as shown in (c2). A given K-bilayer pair may contain
33 many combinations and shapes of Shockley partial dislocations, each with its own
34 transformation rate. As curved dislocations move faster than straight ones lying along the
35 Peierls trough [19,29,34], the case in (c1) should have the smallest transformation rate,
36 whereas the circular loops in (c2) should have the fastest rate. Other cases would have
37 intermediate rates. Here we designate the straight-line glissile Shockley partial dislocation
38 as ‘G-line’ and the circular loop as ‘G-loop’.

39 The Frank–Shockley type dislocation is also required for the transformation. As the
40 Shockley type nucleates randomly, each time transforming two bilayers from K to H, some
41 regions of single K-bilayer will remain. Transforming these single bilayers requires the
42 Frank–Shockley partial dislocations. But these dislocations involve mass transport in both
43 their generation and their motion through the crystal, which means that they are much
44 slower than the Shockley partial dislocations. Moreover, the climb velocity of a
45 Frank–Shockley partial dislocation rapidly decreases as it moves away from the grain

1 boundary or interface due to a larger diffusion path from this interface, which means that a
 2 nucleated Frank–Shockley partial dislocation rapidly turns into a circular loop as shown in
 3 Figure 3(c4). We designate this type of dislocation loop as a ‘C-loop’.

4 The Frank type shown in Figure 2(b) can also contribute to the transformation,
 5 although the process requires three K-bilayers, which then transform into two H-bilayers.
 6 Geometrically and energetically, this seems less likely to occur than that of the
 7 Frank-Shockley type. And as this type cannot annihilate isolated single K-bilayers, we
 8 consider only the Frank–Shockley and Shockley types in the following calculations.

9 3. Results and discussion

10 3.1. Transformation through sub-grain growth

11 We view stacking disordered ice as a sub-grain structure composed of extended
 12 dislocations in hexagonal ice I_h . This structure gradually transforms into a stable state of I_h
 13 via sub-grain growth driven by dislocation reactions. Various dislocation mechanisms and
 14 processes may occur during this growth process, such as described in Section 2.5.1,
 15 although it is difficult to formulate such complicated processes. Instead, here we calculate
 16 the annihilation rate of partial dislocation arrays for the fastest case shown in Figure 7.

17 The four sub-boundaries 1 to 4 in Figure 7 are formed by dissociation from two
 18 perfect dislocations with opposite Burgers vectors \mathbf{a} and $-\mathbf{a}$ lying on the same basal plane.
 19 Each sub-boundary is composed of the same $2N+1$ partial dislocations with the separation
 20 D , and the separations between the sub-boundaries 1 to 2 (also 3 to 4) and 2 to 3 are w_1 and
 21 w_2 , respectively. We now estimate the time required to annihilate the sub-boundaries 2 and
 22 3 at a constant temperature t_g , hereafter the annihilation time, and also the temperature
 23 above which the sub-boundaries 2 and 3 are annihilated within a given duration of
 24 isothermal annealing temperature T_g , hereafter the annihilation temperature. To calculate
 25 these quantities, assume that the sub-boundaries 1 and 4 cannot move outwards, meaning
 26 that $2w_1 + w_2 \leq w_0$, with w_0 being the initial value of the separation between the
 27 sub-boundaries 1 and 4. Also assume that initially $w_1 = w_2 \approx 2ND$, and that sub-grain
 28 growth takes place only by increasing w_1 (thus decreasing in the sub-grain size w_2).

29 Consider the interaction force per unit length $f_{ij}(x)$ exerted on the partial dislocation at
 30 ‘0’ in sub-boundary i from the partial dislocations in the sub-boundary j . This force can be
 31 given by Equation (1), modified to fit a different value of ω . For the case $\omega = 60^\circ$, which
 32 has the maximum attractive force between sub-boundaries 2 and 3, this force $f_{ij}(x)$ is
 33
 34

$$35 \quad f_{ij}(x) = \frac{\mu b_{ie} b_{je}}{2\pi(1-\nu)} \left[\frac{1}{x} + 2 \sum_{n=1}^N \frac{x(x^2 - (nD)^2)}{(x^2 + (nD)^2)^2} \right] + \frac{\mu b_{is} b_{js}}{2\pi} \left[\frac{1}{x} + 2 \sum_{n=1}^N \frac{x}{x^2 + (nD)^2} \right], \quad (3)$$

36 where b_{ie} and b_{is} are the edge and screw components of the partial dislocations in the array
 37 i . Focusing on the sub-boundary 2, the force exerted on the partial dislocation at the centre
 38 of the sub-boundary 2 can be expressed by

$$39 \quad F_2(w_1, w_2) = f_{21}(w_1) - f_{24}(w_1 + w_2) - f_{23}(w_2) - \gamma_{f2}, \quad (4)$$

40 with the edge and screw component $b_p/2$ and $-\sqrt{3}b_p/2$, b_p and 0, $-b_p$ and 0, and $-b_p/2$ and

1 $\sqrt{3}b_p/2$ for $i = 1$ to 4, respectively.

2 Substituting Equation (4) into f of Equation (2), the velocity of the partial dislocation
 3 at the centre of sub-boundary 2 can be obtained by $V_g = MF_2/b_p$. To obtain the fastest case,
 4 the mobility M for curved dislocations (Section 2.5.1) was used in the following
 5 calculation. For simplicity, assume that all partial dislocations comprising sub-boundary 2
 6 move at the same velocity V_g .

7 Then, to estimate t_g , integrate $1/V_g$ for w_2 from the initial value w_2^0 to $w_2^0/2$ and
 8 assume $w_2^0 = 25$ nm, the average initial size in the experiments [13]. We then calculate t_g
 9 as a function of annealing temperature for a given distance D . As a result, when $D = 8c$, the
 10 time equals 33 h at 140 K, 5.7 h at 145 K, 3,800 s at 150 K, 811 s at 155 K, and 188 s at
 11 160 K. In the experiments, annealing occurred for about 2 h, and the crystallite size
 12 increased above 150 K but not at 145 K. Thus, the calculations agree with experiment, with
 13 sub-grain growth occurring above 150 K.

14 We now calculate the annihilation temperature T_g for several cases, again assuming an
 15 annealing time of 2 h. Table 1 shows T_g calculated for sub-grain sizes (i.e. w_2^0) of 25 and
 16 100 nm. This table shows how the annihilation temperature T_g depends on the sub-grain
 17 size w_2^0 , the distance D , and the number N of the partial dislocation array. Specifically, T_g
 18 increases with increasing w_2^0 and D , but with decreasing N ; however, the changes are
 19 small, with T_g changing by only a few degrees near 150 K, even for larger changes in the
 20 parameters. Thus, significant sub-grain growth during laboratory timescales occurs at
 21 about 150 K.

22
 23 Table 1. Annihilation temperature of two partial dislocation arrays with opposite Burgers vectors
 24 by glide motion.

Subgrain size w_2^0 (nm)	Distance D (nm)	Number of partial disl. $2N+1$	Misorient. Angle θ°	Annihilation temperature	
				T_g (K)	T'_g (K)
25		1		151	165
	$8c$ (~5.9)	5	2.5	148	161
	$3c/2$ (~1.1)	21	13.5	144	156
100		1		162	174
	$8c$ (~5.9)	17	2.5	153	167
	$3c/2$ (~1.1)	91	13.5	148	160

25
 26 For the ice I_c formed by depressurization from ice V, the cubicity slightly decreased
 27 from about 0.62 to 0.58 during 9 h of annealing from 150 to 180 K, then decreased to
 28 about 0.27 over 8 h in going from 180 K to 210 K, whereas the crystallite (sub-grain) size
 29 increased from about 25 to 50 nm, whilst annealing up to 180 K followed by an increase to
 30 more than 100 nm during annealing above 180 K [13]. Similar results were found in ice I_c
 31 formed by depressurization from ice IX although the initial cubicity was around 0.4 in this
 32 case. In vapour-deposited ice I_c , Kuhs et al. [1] found a more rapid decrease in cubicity,
 33 going from about 0.45 to 0.1 in an 8-h annealing from 175 to 200 K.

1 In the glide-annihilation model, the stacking faults start annihilating after
 2 sub-boundaries 2 and 3 have completely annihilated. Starting from this time, we calculate
 3 the temperature T'_g for the complete annihilation of a stacking fault between
 4 sub-boundaries 1 and 4. Substituting the attractive force $f_{14} + \gamma_{f2}$ between these sub-bound-
 5 aries into f of Equation (2), the velocity of sub-boundaries 1 and 4 can be obtained by
 6 $V_g = M(f_{14} + \gamma_{f2}) / b_p$. Then, the annihilation temperatures T'_g were calculated by the same
 7 method, and for the same parameters, as those for T_g , and are included in Table 1. The
 8 resulting temperature is about 12–14 K higher than T_g . This result may help explain
 9 observed delay in the annihilation of stacking faults after significant sub-grain growth has
 10 occurred. However, as all these processes with glide motion occur below 180 K (Table 1),
 11 another process or processes must slow the transformation. One such slow, rate-limiting
 12 process may be the motion of the jogged dislocations. However, this motion may not be the
 13 slowest part of the transformation.

14 The slowest process of the transformation is likely the annihilation of extended
 15 dislocations by climb motion. As described in Section 2.5.1, formation of the constricted
 16 bow out is required for this annihilation. The rate-limiting step of this annihilation process
 17 may be the climb motion of the perfect dislocation segment AA' in Figure 10(b). To
 18 estimate this rate, we calculate the time required for two extended dislocations with
 19 opposite Burgers vectors \mathbf{a} with $\omega = \pm 90^\circ$ in a distance r to annihilate each other by the
 20 climb motion of AA'. This climb motion is driven by the attractive force f_y acting on AA'
 21 from two partial dislocations 3 and 4 in (a) (or 3' and 4' in (b)). The climb velocity equals
 22 [22]

$$23 \quad V_c = \frac{2\pi\Omega D_{SD}}{b^2 kT \ln\left(\frac{R_{SD}}{b}\right)} f_y. \quad (5)$$

24 The force f_y (per unit length) is

$$25 \quad f_y(r) = \frac{\mu b^2}{2\pi(1-\nu)} \frac{r \left\{ 3 \left(\frac{w}{2} \right)^2 + r^2 \right\}}{\left\{ \left(\frac{w}{2} \right)^2 + r^2 \right\}^2}, \quad (6)$$

26 where D_{SD} is self-diffusion coefficient, b the Burgers length of the perfect dislocation (i.e.
 27 the lattice constant a), w the separation of the two partial dislocations (i.e. the sub-grain
 28 size), R_{SD} the outer radius for the molecular diffusion, and Ω the molecular volume. The
 29 self-diffusion coefficient is given by

$$D_{SD} = A_{SD} \exp\left(-\frac{E_{SD}}{kT}\right), \quad (7)$$

with $A_{SD} = 1.16 \times 10^{-3} \text{ m}^2/\text{s}$ and $E_{SD} = 0.62 \text{ eV}$ [35,36].

3

4 Table 2. Annihilation temperature of two extended dislocations with opposite Burgers vectors by
5 climb motion.

Sub-grain size w (nm)	Distance ^a D (nm)	Annihilation temperature T_c (K)	
		$R_{SD} = 100 \text{ nm}$	$R_{SD} = 1 \text{ }\mu\text{m}$
25	$16c$ (~11.7)	180	181
	$4c$ (~2.9)	178	179
50	$32c$ (~23.5)	187	189
	$16c$ (~11.7)	186	188
	$4c$ (~2.9)	184	186
100	$64c$ (~47.0)	196	198
	$16c$ (~11.7)	193	195
	$4c$ (~2.9)	191	193

6 ^aNote the distance D , which corresponds to the length A'B' in Figure 10(c), includes a jog height
7 A₀B' in (b).

8

9 To compare with experiments by Hansen et al. [13], the annihilation temperature T_c
10 was determined for an annealing time of 2 h. In this calculation, the annihilation time t_c
11 was calculated by integrating $1/V_c$ for r from D to 0, assuming the cases of R equal to 100
12 nm and 1 μm . The calculated results in Table 2 show that annihilation by climb becomes
13 active above about 180 K. The annihilation temperature T_c decreases by only a few degrees
14 when D decreases by one order of magnitude, but increases by more than 10 K when the
15 sub-grain size increases from 25 to 100 nm.

16 In the experiments, the crystallite (sub-grain) size at 180 K is around 50 nm. For this
17 size, the present model predicts annihilation as the temperature increases above a T_c of
18 184–187 K. After the possible dislocation reactions occur, dislocations of various shapes,
19 including faulted dislocation loops, must remain. The resulting cubicity will be roughly
20 proportional to the dislocation density. To annihilate all stacking faults, all dislocations
21 would have to be removed from ice sample, which cannot occur. Thus, the resulting
22 hexagonal ice I_h will contain some cubic stacking sequences.

23

24 **3.2. Transformation through annihilation of stacking faults**

25 Consider the transformation rate on annealing (or ageing) the grain structure described in
26 Section 2.5.3 and also shown in Figure 6(b). Two cases are analysed, that with Shockley
27 partial dislocations, and that with Frank-Shockley partial dislocations.
28

29

30 **3.2.1. Transformation by Shockley partial dislocations**

31 The shrinking of a glissile Shockley partial dislocation loop (G-loop) is likely the fastest
32

1 annihilation process in the transformation. For this reason, we consider it an upper bound
 2 of the transformation rate. In this case, the driving force f in Equation (2) for a faulted
 3 dislocation loop of radius r equals

$$\begin{aligned}
 F_g &= \frac{1}{r} \frac{\mu}{4\pi(1-\nu)} \frac{2-\nu}{2} b_p^2 \left[\ln \left(\frac{8\alpha r}{b_p} \right) - 1 \right] + \gamma_{f2} \\
 &\approx \frac{(2-\nu)}{8\pi(1-\nu)} \frac{\mu b_p^2}{r} \ln \left(\frac{8\alpha r}{b_p} \right) + \gamma_{f2} \quad (\text{for } 8\alpha r \gg b_p)
 \end{aligned}
 \tag{8}$$

5 where ν is Poisson's ratio, μ the shear modulus, b_p the Burgers vector length, and α a core
 6 parameter [22]. Then, we obtain the shrinkage rate of G-loop $|\dot{r}|$ as

$$|\dot{r}| = V_g \approx M \left\{ \frac{2-\nu}{8\pi(1-\nu)} \frac{\mu b_p}{r} \ln \left(\frac{8\alpha r}{b_p} \right) + \frac{\gamma_{f2}}{b_p} \right\}. \tag{9}$$

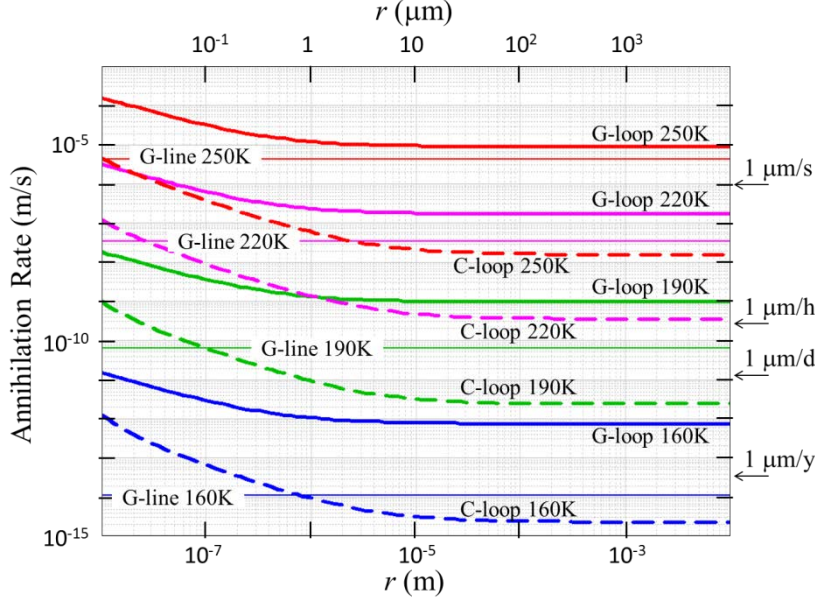
8 Substitution of $M_0 = 14.5 \text{ m/s}\cdot\text{Pa}$, $E_g = 0.624 \text{ eV}$ for a curved dislocation, $\gamma_{f2} = 0.62 \text{ mJ/m}^2$,
 9 $\nu = 0.325$, $\alpha = 1.7$ and values of b_p and μ at different temperatures [35,36] produces the
 10 shrinkage rates at 160–250 K shown in Figure 13.

11 The resulting shrinkage rate of G-loops increases rapidly as the loop radius r decreases
 12 below $1 \mu\text{m}$, due to the first $1/r$ term. But at larger r , the second constant term on the right
 13 side of Equation (9) dominates the rate, and the shrinkage rate becomes constant. At a
 14 fixed r , the shrinkage rate is sensitive to temperature. For example, with an initial
 15 loop-radius (or grain radius) of $5 \mu\text{m}$, the transformation of bilayers is completed within
 16 one second at 250 K, but over a month at 160 K.

17 For the lower bound of the transformation rate from the Shockley partial dislocation,
 18 we consider the sweep by a straight 30° -partial dislocation across the ice grain. This case is
 19 considered because such a dislocation would arise from a perfect screw dislocation, and a
 20 screw dislocation moves much slower than other perfect dislocations [19,29]. When a
 21 straight 30° -partial dislocation lies along the Peierls trough (i.e., parallel to \mathbf{a}), as shown in
 22 Figure 12(c1), the velocity of the Shockley partial dislocation has a minimum, being equal
 23 to the second term in Equation (9): $V_{30} = (\gamma_{f2} / b_p) M_0 \exp(-E_g/kT)$. Substituting $E_g = 0.756$
 24 eV and $M_0 = 3.0 \times 10^3 \text{ ms}^{-1}\text{Pa}^{-1}$, the values of V_{30} (G-lines) at 160–250 K, one gets the
 25 values shown in Figure 13. In this calculation, the value M_0 was set to twice the value
 26 obtained for a perfect screw dislocation because it dissociates into two 30° -partial
 27 dislocations.

28 As a result, the annihilation rates of the stacking faults by the Shockley partial
 29 dislocations distribute between the horizontal G-line (lower bound) and the G-loop curve
 30 (upper bound) at a given temperature in Figure 13. A wider range occurs at lower
 31 temperatures. For a grain radius (i.e. an initial G-loop radius) exceeding $10 \mu\text{m}$, the
 32 annihilation rates range over two orders of magnitude at 160 K but are within the same
 33 order of magnitude at 250 K. The change is due to the difference in E_g for curved
 34 dislocations and straight dislocations, and this difference is due to the kink formation
 35 energy required to move the straight dislocation lying along the Peierls trough [19,29]. For

1 smaller grain radii, the difference in the annihilation rate between lower and upper bound
 2 increases with decreasing radius due to the increasing driving force f for G-loops with
 3 smaller r .



4

5 Figure 13. Annihilation rates of stacking faults by glide motion of Shockley partial dislocations
 6 (G-loops and G-lines) and by climb motion of Frank–Shockley partial dislocations (C-loops) as
 7 functions of radius r and for four values of temperature.

8

9

10 3.2.2. Transformation by Frank–Shockley partial dislocations

11 The second transformation mechanism to consider is the shrinkage of a Frank–Shockley
 12 partial dislocation loop (C-loop) (see Figure 12(c4)). The driving force for shrinkage of
 13 this type is
 14

$$15 \quad F_C \approx \frac{\mu}{4\pi(1-\nu)r} \left\{ \frac{2-\nu}{2} b_p^2 \ln \left(\frac{8\alpha r}{b_p} \right) + b_n^2 \ln \left(\frac{8\alpha r}{b_n} \right) \right\} + \gamma_{fl} \quad (10)$$

16 where b_p and b_n are the parallel and normal components of the Burgers vector to the basal
 17 plane [20], $b_p = p_i = a/\sqrt{3}$ and $b_n = c/2$.

18 For diffusion-controlled dislocation climb, the shrinkage rate of a C-loop can be
 19 expressed by

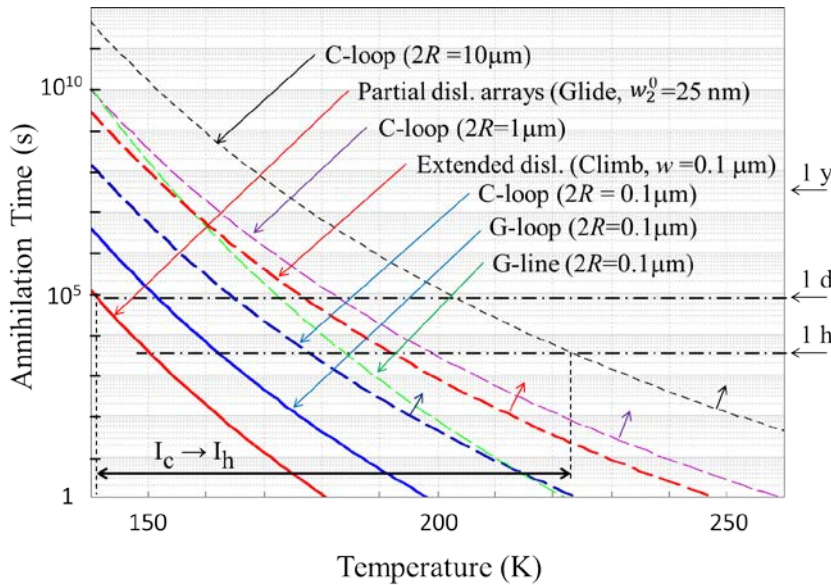
$$20 \quad |\dot{r}| = \beta \frac{D_{SD}}{b_n} \left[\exp \left(\frac{F_C \Omega}{kT b_n} \right) - 1 \right] \quad (11)$$

21 where D_{SD} is the self-diffusion coefficient, Ω the molecular volume and β the geometrical

1 factor [37]. When the radius r of the C-loop is small compared with the grain radius, we
 2 can assume spherical symmetry, solve the diffusion equation, and obtain $\beta = 2$ [37]. For
 3 large r , β should be smaller than 2 although it exceeds 2 for r very close to R (within a few
 4 nm in the present case). To obtain the lower bound of the annihilation time (i.e., upper
 5 bound for the shrinkage rate), we assume this value of 2 applies to large r ($\approx R$). If D_{SD} is
 6 given by Equation (7) with values for b_p , b_n , ν , α , and μ all being the same as those for the
 7 G-loop, then one gets the shrinkage rates of C-loops plotted in Figure 13. The shrinkage
 8 rates of the C-loops are more than two orders of magnitude less than those of the G-loops,
 9 but become larger than the lower bound (G-lines) at smaller radius r .

11 3.3. Annihilation time of the stacking faults

12 To address the calculated annihilation times of the stacking faults, we first examine the
 13 annihilation times for the partial dislocation arrays by glide motion t_g and for the extended
 14 dislocations by climb motion t_c . The results are plotted in Figure 14. The solid red curve
 15 shows t_g calculated for the initial sub-grain size of 25 nm as the fastest case, and the dashed
 16 red curve shows t_c calculated for the sub-grain size of 0.1 μm as the slowest case. That is,
 17 the transformation from I_c to I_h by this mechanism would start between these two red
 18 curves, and continue to a higher temperature until the sub-boundary network breaks up.



21 Figure 14. Temperature-dependent annihilation time for both transformation mechanisms
 22 (through sub-grain growth and stacking fault annihilation). Annihilation times for G-loops with $2R$
 23 of 1 μm and 10 μm (not shown here to avoid confusion) are close to those for C-loops with $2R$ of
 24 0.1 μm (dashed blue curve) and for extended dislocations by climb with w of 0.1 μm (dashed red
 25 curve), respectively. The transformation of I_c to I_h can be observed in a wide temperature range
 26 indicated by the double-armed solid line between 141 and 223 K for the annihilation by the
 27 different mechanisms on possible grain sizes within the typical laboratory timescale from an hour
 28 to a day. This temperature range would extend to higher temperatures as indicated by the short
 29 arrowed lines because these dashed lines for climb mechanisms correspond to the lower bound of
 30 the annihilation time.

1 In the transformation through annihilation of stacking faults, we use these annihilation
2 rates for G-loops, G-lines, and C-loops to calculate the annihilation times of the stacking
3 faults. For the calculation, we integrate the inverse of the shrinkage rates using the
4 temperature-range-averaged values for the shear modulus and lattice constants. Initially,
5 the loop will encircle the entire grain, which will be assumed to have a diameter of 0.1, 1.0
6 or 10 μm . The straight 30° -partial dislocation, on the other hand, will sweep the entire
7 grain, maintaining a straight alignment along the Peierls trough.

8 The resulting annihilation times decrease rapidly with increasing temperature as
9 shown in Figure 14. The solid blue curve shows the annihilation time calculated for a
10 G-loop of initial diameter 0.1 μm as the fastest case in the transformation mechanism, and
11 the dashed blue curve shows that for a C-loop of the same initial diameter. For such a small
12 loop, Figure 13 shows that the annihilation rate by a G-line becomes smaller than that by a
13 C-loop at low temperatures. Then, I_c samples with a grain size of about 0.1 μm would start
14 to transform in a temperature range between the solid blue curve and the dashed green
15 curve by this mechanism. In contrast, if the grain size is 10 μm , the transformation would
16 occur between the dashed red curve and the dashed black curve.

17 However, as discussed in Section 2.5.3, the nucleation rate of C-loops must be much
18 smaller than that of G-loops. Then, the transformation by C-loops may continue to a higher
19 temperature until C-loops nucleate on the remaining K-bilayers. Therefore, the annihilation
20 times of C-loops (dashed blue and black curves) should be viewed as the lower bound for
21 the transformation by C-loops.

22 As a real I_c sample must include grains of various sizes and sub-boundary structures,
23 the range of transformation times in Figure 14 suggests that the transformation should
24 occur over a wide temperature range. Moreover, the grain sizes and sub-structures must
25 depend on the method by which the I_c sample was formed, with variation from sample to
26 sample, even if formed by the same method. (Similar arguments may explain the wide
27 scatter in the heat of transformation, as discussed in more detail in the next section.)
28 Finally, considering that the typical laboratory timescale may vary from an hour to a day,
29 the possible transformation temperature range should be wide, estimated at 141–223 K as
30 indicated in Figure 14.

31 This estimated range is consistent with the start of the observed transformation
32 temperatures [1,13,16,17,38]. Specifically, Table 3 shows that the temperature T_i at which
33 the transformation appeared to start ranges within 150–182 K, and the temperatures T_f at
34 which the transformation appeared to end ranges within 210–225 K. These experimental
35 results can fit the calculated temperature range if the grain sizes range from 25 nm to 10
36 μm in these different experiments. But, what are the grain sizes? The calorimetric
37 experiments did not report them, but the sizes can be assumed to equal those found in
38 diffraction experiments done on similarly prepared I_c samples, which are close to 0.1 μm .
39 With such a grain size, the calculated results shown in Figure 14 is roughly consistent with
40 the temperature range for T_i , although the observed T_f is much higher than the calculated
41 temperature range for 0.1 μm . That is, the transformation continues to a much higher
42 temperature than expected. However, the annihilation times calculated for the slowest case
43 considered for each mechanism should be viewed as a lower bound. The actual
44 transformation should continue to a higher temperature due to dislocation reactions that

1 break up the sub-boundary network and also due to delayed nucleation of C-loops.

2 The results are also consistent with experiments at a constant temperature. Specifically,
3 for vapour-deposited ice, Kuhs et al. [1] found a nearly complete transformation (to
4 cubicity ≤ 0.05) within 6 hours at 185 K, but an incomplete transformation (to cubicity
5 ~ 0.3) after 10 hours at 175 K. By extrapolating their decreasing curve at 175 K, it would
6 take about 40 hours ($\approx 1.4 \times 10^5$ s) to complete the transformation at this temperature. These
7 rates agree with the annihilation time of extended dislocations by climb with $w = 0.1 \mu\text{m}$
8 (dashed red curve in Figure 14), which is consistent with the SEM micrographs of the ice
9 showing a sub-micron grain structure, with grain sizes as small as 50–200 nm [1].

10 A complete transformation requires the annihilation of C-loops. These annihilation
11 times are much longer than those for G-loops; indeed, below 180 K, a complete
12 transformation would take several days for a grain size of $1 \mu\text{m}$. Consequently, annealing
13 at a higher temperature is needed to complete the transformation within experimentally
14 practical times. Consistent with this prediction, Kuhs et al. [1] reported that the cubicity
15 decreased from about 0.5 to 0.05 within several hours at 185 K, but some cubic stacking
16 sequences disappeared only upon heating to 240 K. Finding that stacking faults
17 disappeared at 240 K was first reported by Kuhs et al [39]. Later, Falenty et al. [38] also
18 reported a similar result. Figure 14 indicates that the G-loops with a diameter of $10 \mu\text{m}$
19 should vanish within 220 s at 205 K whereas more than 16 h is needed for the C-loops, and
20 the remaining C-loops can be annihilated within 400 s at 240 K if the nucleation time can
21 be ignored. For a grain size below $1 \mu\text{m}$, the C-loops should vanish completely within a
22 second at 240 K, but take 1,200 s at 205 K and more than a half day at 185 K.

1 Table 3. Transformation temperatures for I_c to I_h depending on experimental methods.

2

Experimental method			Sample	Transformation temperature ^a			Reference	
				Grain size	T _i (cubicity)	T _f (cubicity)		
Calorimetry	Continuous heating	10 K/h	Depressurization from high pressure phase	II, IX, V, VI, VIII	—	182 ± 5 K (Averaged over 14 runs)	224 ± 6 K	[16]
	Stepped heating	1 h, 2.3 K		IX	—	165 K	225 K	[17]
Diffraction		2 h, 10 K		V	25–200 nm	150 K (0.62)	210 K (0.26)	[13]
				IX	20–150 nm	150 K (0.42)	210 K (0.2)	
		2 h, 5 K		V		—	—	[1]
				IX		175 K (0.581) ^b	185 K (0.555) ^b	
			Vapour deposited		70–120 nm	~165 K	~210 K	
						175 K (0.385) ^b	185 K (0.365) ^b	
			From CO ₂ -hydrate		~5 μm	~170 K	~210 K	
						175 K (0.278) ^b	185 K (0.051) ^b	
						175 K (0.422) ^b	185 K (0.137) ^b	
	Iso-thermal	≤16 h			2–10 μm	167.7 K	240 K	[38]

3 ^a T_i and T_f are the temperatures at which the transformation appeared to start and end, respectively.

4 ^b Temperature at which the cubicity was obtained.

*Email: hondoh@general.hokudai.ac.jp

†Present address: Professor emeritus at Hokkaido University, 2-2-107, 5-8 Hassamu, Nishi-ku Sapporo, 063-0825 Japan.

3.4. *Anomalously wide range in measured heat of transformation*

The energy difference, or enthalpy of transformation, ΔU_{CH} between I_{h} and I_{c} range widely, from 13 to 50 J/mol, due apparently to differing methods by which the I_{c} crystal was formed [16]. But how exactly did the formation method affect the grain structure?

We can understand this wide range in ΔU_{CH} as a result of the different formation processes producing different densities and arrangements of dislocations. The transformation to stable hexagonal ice may occur through several modes; for example, sub-grain growth including complicated reactions among partial dislocations as well as perfect dislocations (see Section 3.1), or through annihilation of stacking faults by partial dislocations sweeping the faulted basal planes (see Section 3.2).

In the former case, the transformation releases the stored energy in the dislocations E_{d} . As E_{d} for a dislocation density ρ_{d} can be approximately expressed by $E_{\text{d}} \approx \rho_{\text{d}} \mu b^2 / 2$, we obtain 78 J/mol for the high dislocation density ρ_{d} of 10^{16} m^{-2} , which is the maximum of the energy release by the transformation from pure I_{c} to I_{h} , and thus the upper bound for ΔU_{CH} measured by experiment. But such a high density of dislocations would quickly rearrange into a stable array, the ice would then be in a lower stored energy state when measurements start. Therefore, a lower energy release would be obtained.

In the latter case, on the other hand, only stacking faults are left after absorption of partial dislocations by high-angle grain boundaries or interfaces. As I_{c} is composed of only K-bilayers with spacing $c/2$, the energy difference ΔU_{CH} between I_{h} and I_{c} should equal $2\gamma_{\text{fl}}/c$ per unit volume. This gives $\Delta U_{\text{CH}} \approx 16 \text{ J/mol}$, a value close to the lowest value measured of 13 J/mol. In this case also, the starting material used for the measurements has already partly transformed when the measurements start, suggesting a value below 16 J/mol.

The density and arrangement of dislocations introduced into a crystal in general strongly depends on the stress field exerted on the crystal and the thermal history of the crystal. From these variable factors, through their effect on the dislocation-fault structure, comes the likely source of the widely scattered heats of transformation from I_{c} to I_{h} .

3.5. *Stability of the stacking-disordered state*

To understand the particular nature of stacking disordered state in ice I_{h} , consider the behaviour of dislocations at an elevated temperature. Although the cubicity of aged ice I_{h} , which is proportional to a density of dislocations, may be below 10^{-4} as described in Section 2.3, cubicity would be increased by heat treatment in a temperature range at which the concentration of self-interstitials is high enough to generate dislocation loops. When self-interstitials in thermal equilibrium at melting temperature (mole fraction 2.8×10^{-6} [19,40]), segregate into faulted dislocation loops of Frank–Shockley type, the cubicity increases by at most 0.028. If they segregate into those of Frank type, the value becomes 0.084. In fact, very many faulted loops generated by both cooling and heating were observed in single crystals of ice by x-ray diffraction topography [20,23,41]. By cooling, supersaturated self-interstitials segregate into faulted loops, and by heating, on the other hand, faulted loops of vacancy type are generated to supply self-interstitials into the crystal undersaturated with self-interstitials. In addition, due to ice's anisotropic thermal expansion, dislocations can also be generated in polycrystalline ice by thermal stresses during heat

1 treatment. These dislocations will dissociate into partial dislocations that bound stacking
2 faults (e.g., when N_t partial dislocations form an array as discussed in Section 2.3, these
3 fault widths will be roughly equal to $N_t \times w_e$). Therefore, both cooling and heating can
4 increase the stacking disorder. Moreover, if ice is formed from supercooled water, excess
5 self-interstitials introduced by density reduction at freezing would increase the stacking
6 disorder.

7 The complex behaviour of the stacking disorder in ice discussed by Malkin et al. [14]
8 may be understandable if we consider the above behaviour of dislocations at an elevated
9 temperature. As a result of the nature and behaviour of self-interstitials and dislocations in
10 ice I_h , the complex behaviour of the stacking disorder may arise from the route of
11 formation and thermal history, not necessarily from the unknown complexity of ice
12 suggested by Malkin et al. [14].

13 An anomalous stability of the stacking-disordered state was found by Morishige et al.
14 [42,43] in their x-ray diffraction measurements on ice formed by the freezing of water
15 confined in mesopores of pore-size 4–70 nm. Ice formed by freezing the pore water at 261
16 K shows the typical I_c diffraction pattern. No other experimental methods, including
17 depressurization, produce I_c crystals at this temperature. The mesopore ice I_c is thermally
18 stable; for example, in case of cylindrical pores of diameter 8 nm, the ice remains stable up
19 to the melting point of the ice. Such anomalous stability was not observed in the case of
20 spherical pores of diameter 10–17 nm.

21 The pores, being comparable or smaller than w_e (57 nm), should increase the I_c
22 fraction according to the present formation mechanism. First, a high density of dislocations
23 must be introduced by deformation and supersaturated self-interstitials upon freezing in a
24 confined space. Then, to stabilize the stacking-disordered state at such a high temperature,
25 adhesion between ice and the pore material should be strong enough to avoid absorption of
26 the partial dislocations at the interface. Thus, the partial dislocations bounding the stacking
27 faults remain stuck at the interface, preventing the generation of other partial dislocations
28 by which the stacking fault will be annihilated.

29 Anisotropic stresses on the ice, which likely depend on pore shape, may alter the
30 dominant Burgers vectors. For example, compressive (or tensile) stress parallel to the
31 c -axis produces dislocations mainly with Burgers vector $a+c$, whereas dislocations with
32 Burgers vector a dominate under other stresses. Both types of dislocations extend on the
33 basal plane, but climb motion is required for movement of partial dislocations dissociated
34 from the Burgers vector $a+c$. Such difference in behaviour of dislocations may affect the
35 stability of the stacking disordered state although we do not yet know the details of the
36 mechanism.

37 38 **4. Summary and conclusions**

39
40 The structures of stacking disorder in cubic ice I_c has been revealed experimentally
41 [13–15,26], but its formation mechanism remains an open question. Here, a mechanism
42 involving partial dislocations has been presented to explain the formation of cubic ice I_c ,
43 including partly cubic or stacking-disordered ice, and its transformation to hexagonal ice I_h .
44 This dislocation mechanism is based on the experimentally determined crystallite sizes of
45 I_c [13,26] because these sizes are comparable to the equilibrium widths of extended

1 dislocations in hexagonal ice I_h . The mechanism predicts two stacking-disordered
2 structures, and their transformation through different dislocation processes.

3 In fine-grained polycrystalline ice with a high density of dislocations, widely
4 extended dislocations produce the stacking disordered state. The partial dislocations that
5 bound the stacking faults rearrange into stable arrays or sub-boundaries around a sub-grain
6 structure containing cubic and hexagonal stacking sequences. This stacking-disordered
7 structure has a relatively high amount of stored energy, and because it has a high density of
8 extended dislocations, the transformation to ice I_h occurs through dislocation reactions.

9 Another polycrystalline ice with stacking disorder can be formed if the temperature is
10 high enough for the high-angle grain boundaries (or, at lower temperature, if binding
11 between grains in powdered ice is weak enough), to act as sinks for dislocations. In this
12 case, the partial dislocations that bound the stacking faults are absorbed, resulting in a
13 lower stored-energy state of stacking-disordered ice. For the transformation of this state to
14 ice I_h , the dislocation mechanism predicts a two-step process consisting of the relatively
15 fast motion of Shockley partial dislocations followed by the relatively slow motion of
16 Frank–Shockley partial dislocations. The first step converts most of the crystal to
17 hexagonal stacking and occurs relatively rapidly, leaving only the slower second step to
18 complete the transformation.

19 Coming from either the high- or low-stored energy state, the transformation process can
20 be thought as a recovery process of a heavily deformed crystal. According to this view, the
21 heat of transformation obtained by calorimetric measurements must be due to the recovery
22 of unstable substructures formed by dislocations. For the heat of transformation, the
23 dislocation mechanism developed here predicts a wide range of values, and a slow
24 transformation occurring over a wide temperature range, both predictions in agreement
25 with experiments. Consequently, the characteristic nature of dislocations in hexagonal ice
26 I_h should be considered when studying cubic ice I_c .

27 These stacking-disordered structures vary with the particular starting phase of ice
28 (high-pressure forms of ice, amorphous ice or gas hydrates) as discussed in the literature
29 [13,15,26]. Further study will be needed to refine the model to accurately describe the
30 transformation from specific structures.

31 **Acknowledgements**

32 I thank Dr. W. F. Kuhs for valuable information on recent research. I also appreciate Dr. J. Nelson
33 for his careful reading of the manuscript and valuable comments that improved the quality of this
34 paper.
35

36 **Disclosure statement**

37 No potential conflict of interest was reported by the author.
38

39 **Funding**

40 This study was partly supported by Creative Scientific Research [grant number 14GS0202]
41 provided by the Ministry of Education, Culture, Sports, Science and Technology (MEXT).
42
43

44 **ORCID**

45 *T. Hondoh*  <http://orcid.org/0000-0003-4129-022X>

References

- [1] W.F. Kuhs, C. Sippel, A. Falenty and T.C. Hansen, Proc. Natl. Acad. Sci. USA, 109 (2012) p.21259.
- [2] T.L. Malkin, B.J. Murray, A.V. Brukhno, J. Anwar and C.G. Salzmann, Proc. Natl. Acad. Sci. U S A, 109 (2012) p.1041.
- [3] E. Whalley, J. Phys. Chem., 87 (1983) p.4174.
- [4] D.M. Murphy, Geophys. Res. Lett., 30 (2003) p.2230.
- [5] T. Peter, C. Marcoli, P. Spichtinger, T. Corti, M.B. Baker and T. Koop, Science, 314 (2006) p.1399.
- [6] B.J. Murray, D.A. Knopf and A.K. Bertram, Nature, 434 (2005) p.202.
- [7] J.E. Shilling, M.A. Tolbert, O.B. Toon, E.J. Jensen, B.J. Murray and A.K. Bertram, Geophys. Res. Lett., 33 (2006) p.L17801.
- [8] T. Bartels-Rausch, V. Bergeron, J.H.E. Cartwright, R. Escibano, J.L. Finney, H. Grothe, P.J. Gutierrez, J. Haapala, W.F. Kuhs, J.B.C. Pettersson, S.D. Price, C. Ignacio Sainz-Diaz, D.J. Stokes, G. Strazzulla, E.S. Thomson, H. Trinks and N. Uras-Aytemiz, Reviews of Modern Physics, 84 (2012) p.885.
- [9] A. Kouchi, T. Yamamoto, T. Kozasa, T. Kuroda and J.M. Greenberg, Astronom. Astrophys., 290 (1994) p.1009.
- [10] R.S. Smith, C. Huang, E.K.L. Wong and B.D. Kay, Phys. Rev. Lett., 79 (1987) p.909.
- [11] T. Takahashi, J. Cryst. Growth, 59 (1982) p.441.
- [12] G.P. Johari, J. Chem. Phys., 122 (2005) p.194504.
- [13] T.C. Hansen, M.M. Koza, P. Lindner and W.F. Kuhs, J. Phys.: Condens. Matter, 20 (2008) p.14.
- [14] T.L. Malkin, B.J. Murray, C.G. Salzmann, V. Molinero, S.J. Pickering and T.F. Whale, Phys. Chem. Chem. Phys., 17 (2015) p.60.
- [15] T.C. Hansen, C. Sippel and W.F. Kuhs, Z. Kristallogr., 230 (2014) p.75.
- [16] Y.P. Handa, D.D. Klug and E. Whalley, Can. J. Chem., 66 (1988) p.919.
- [17] O. Yamamuro, M. Oguni, T. Matsuo and H. Suga, J. Phys. Chem. Solids, 48 (1987) p.935.
- [18] A. Fukuda, T. Hondoh and A. Higashi, J. Phys-Paris, 48 (1987) p.163.
- [19] T. Hondoh, in: T. Hondoh (Ed.) *Physics of ice core records*, Hokkaido University Press, Sapporo, 2000, pp. 3-24. Available: <http://eprints.lib.hokudai.ac.jp/dspace/handle/2115/32459>
- [20] T. Hondoh, T. Itoh, S. Amakai, K. Goto and A. Higashi, J. Phys. Chem., 87 (1983) p.4040.
- [21] T. Hondoh, Low Temp. Sci., vol. 68: Supplement Issue, *Physics of ice core records II* (2009) 1, Available: <http://eprints.lib.hokudai.ac.jp/dspace/handle/2115/45404>,
- [22] J.P. Hirth and J. Lothe, *Theory of dislocations*, McGraw-Hill Book Company, 1968.
- [23] T. Hondoh, T. Itoh and A. Higashi, Jpn. J. Appl. Phys., 20 (1981) p.L737.
- [24] K. Goto, T. Hondoh and A. Higashi, Jpn. J. Appl. Phys., 25 (1986) p.351.
- [25] T. Hondoh, K. Azuma and A. Higashi, J. Phys-Paris, 48 (1987) p.183.
- [26] W.F. Kuhs, C. Sippela, A. Falenty and T.C. Hansen, Proc. Natl. Acad. Sci. USA, 109 (2012). Supporting Information Available at www.pnas.org/lookup/suppl/doi:10.1073/pnas.1210331110/-/DCSupplemental.
- [27] J. Weiss and D. Marsan, Science, 299 (2003) p.89.
- [28] A.N. Stroh, Proc. Phys. Soc., B 67 (1954).
- [29] Y. Okada, T. Hondoh and S. Mae, Phil. Mag. a, 79 (1999) p.2853.
- [30] H. Yamakami, A. Goto, T. Matsuyama, P. Kinpara and T. Hondoh, in: N. Maeno and T. Hondoh (Eds.) *Int. Symp. Physics and Chemistry of Ice.*, Hokkaido University Press, Sapporo, 1992, pp. 511-512.
- [31] K. Wessel and H. Alexander, Phil. Mag., 35 (1977) p.1523.
- [32] B. Geil, T.M. Kirschgen and F. Fujara, Phys. Rev. B, 72 (2005) p.10.
- [33] F.J. Humphreys and M. Hatherly, *Recrystallization and related annealing phenomena*, Elsevier, 2004.

- 1 [34] T. Hondoh, in: N. Maeno and T. Hondoh (Eds.) *Int. Symp. on Physics and Chemistry of Ice.*,
2 Hokkaido University Press, Sapporo, 1992, pp. 481-487.
- 3 [35] R.O. Ramseier, *J. Appl. Phys.*, 38 (1967) p.2553.
- 4 [36] V.F. Petrenko and R.W. Whitworth, *Physics of Ice*, Oxford University Press, New York, 1999.
- 5 [37] P.S. Dobson, P.J. Goodhew and R.E. Smallman, *Phil. Mag.*, 16 (1967) p.9.
- 6 [38] A. Falenty, T.C. Hansen and W.F. Kuhs, in: Y. Furukawa, G. Sazaki, T. Uchida and N. Watanabe
7 (Eds.) *Physics and Chemistry of ice*, Hokkaido University Press, Sapporo, 2010, pp. 411-419.
- 8 [39] W.F. Kuhs, G. Genov, D.K. Staykovaa and T. Hansen, *Phys. Chem. Chem. Phys.* , 6 (2004) p.4917.
- 9 [40] K. Goto, T. Hondoh and A. Higashi, in: J. Takamura, M. Doyama and M. Kiritani (Eds.) *Point*
10 *defects and defect interactions in metals*, University of Tokyo Press, 1982.
- 11 [41] T. Hondoh, *Radiat. Eff. Defect. S.*, 124 (1992) p.139.
- 12 [42] K. Morishige and H. Uematsu, *J. Chem. Phys.*, (2005) p.044711.
- 13 [43] K. Morishige, H. Yasunaga and H. Uematsu, *J. Phys. Chem. C*, 113 (2009) p.3056.
- 14